Unterschrift Betreuer

**TECHNISCHE
UNIVERSITÄT
WIEN**
Vienna University of Technology

DIPLOMARBEIT

Systematic Tests for Gravitational Resonance Spectroscopy

zur Erlangung des akademischen Grades

Diplom-Ingenieur

im Rahmen des Studiums

Technische Physik

ausgeführt am Atominstitut
der Technischen Universität Wien

unter der Anleitung von
**Univ.Prof. Dipl.-Phys. Dr.rer.nat. Hartmut Abele
Mag.rer.nat. Dr.techn. René Sedmik**

durch

Lukas Achatz B.Sc.

Am Heumarkt 29/18
1030 Wien

December 17, 2018

Unterschrift Student

Zusammenfassung

Im Rahmen dieser Diplomarbeit wurde ein wichtiger Beitrag zur Gravitationsresonanzspektroskopie von ulrakalten Neutronen mit Hilfe der sogenannten Ramsey Methode geliefert. Diese ultrakalten Neutronen, welche als Nebenprodukt aus der Kernspaltung im Forschungsreaktor am *Institut Laue Langevin* (ILL) in Grenoble entstehen, wandern über ebene Spiegel zu einem ortsauflösenden Detektor. Die Spiegel können über Oszillationen die Neutronen in einen höheren Energiezustand anregen. Anschließend kann die Zustandsverteilung und die Energie der Neutronen im peV Bereich bestimmt werden.

Um möglichst präzise Übergänge zwischen den Energieniveaus zu ermöglichen, ist ein fundiertes Wissen über die Zustandsverteilung nach jeder Region von enormer Bedeutung. Hierfür wurden im Rahmen dieser Diplomarbeit drei verschiedene Absorber Konfigurationen untersucht und anschließend die Zustandsverteilung bestimmt. Die Werte für die Besetzungswahrscheinlichkeiten liegen für den ersten Zustand im Bereich von 46.6 - 60.7 %, für den zweiten Zustand von 38.2 - 44.3 %, für den dritten Zustand von 0.0 - 15.6 % und für den vierten Zustand von 0.0 - 13.7 %.

Zudem wurde der Zusammenhang zwischen Ätzdauer der Detektoren und Anzahl an detektierten Neutronen analysiert sowie die Divergenz des Strahlrohres abgeschätzt.

Abstract

In the scope of this master thesis an important contribution to the so called gravitational resonance spectroscopy from ultracold neutrons using Ramsey's method of separated oscillating fields was given. The Ultra Cold Neutrons (UCNs), produced by the research reactor at the *Institute Laue Langevin* (ILL), travel over plane mirrors to a detector with spatial resolution. With this detector the state occupation and subsequently the energy of the neutrons can be investigated in the peV regime.

In order to achieve precise transitions between the energy eigenstates, an important aspect is the knowledge of the Eigenstate distribution after each region. For this, several absorber configurations are investigated and furthermore the state occupation distribution is determined. The obtained values for the occupation probabilities for the first state are located in the range of 46.6 - 60.7 %, for the second state 38.2 - 44.3 %, for the third state 0.0 - 15.6 % and for the fourth state 0.0 - 13.7 %.

In addition the correlation between etching-time of the detectors and the count of detected neutrons is analysed as well as the divergence of the neutron-beam coming from the beam-line.

Contents

1 Introduction

In our current understanding there are four known fundamental forces in our universe. Gravitation, strong and weak nuclear forces and the electromagnetic force. For the last century many physicists have been trying to combine those four forces into one theory of everything. While the last three are described by the standard model (SM) as gauge theories, gravitation is described as a geometric theory by general relativity (GR) [1]. This fact makes the combination of both SM and GR one of the most difficult tasks in modern physics.
Although GR is widely accepted and has passed countless experimental tests, there are still some problems which lack explanation. GR does not, for example, give an explanation for the rather linear dependency of the rotational velocity of galaxies as a function of the radius as shown in [2]. This discrepancy can be explained with the introduction of additional, invisible matter which hardly interacts with the forces in the SM, thus being called dark matter [3] [4]. Other theories predict new particles like the massless axion (responsible for dark matter) [5] or a chameleon field (responsible for dark energy) [6].

Since gravitation was the first force with a coherent mathematical description, there are numerous experiments testing it on different length and time scales, from cosmology to the microcosm. As explained in [7] higher dimensional gravity theories or massive scalar fields need a more general expression of the Newtonian gravity potential by including a Yukawa term, as can be seen in equation 1.1:

$$V(r) = -G\frac{m_i \cdot m_j}{r}(1 - \alpha \cdot e^{-\frac{r}{\lambda}}). \tag{1.1}$$

Where λ parametrizes the coupling strength, G the gravitational constant and α being a strength factor in units of Newtonian gravity.

Within the qBOUNCE experiment it is possible to test deviations from this potential at small length ($\backsim$ μm) and ultra low energy scales ($\backsim$ peV). This is done by using ultracold Neutrons (UCNs) supplied by the research reactor at the *Institute Laue-Langevin* (ILL)[1]. This is the research reactor with the most intense continuous neutron flux, with a thermal power of up to 58 MW. It was founded

---

[1]Institute Laue-Langevin, 71 Avenue des martyrs, 38000 Grenoble, France

in 1967 by a collaboration of Germany and France and has enabled a long list of successful experiments in a wide range of scientific fields from fundamental physics to structural biology. Since there is only one fuel element of ^{235}U in use, it has to be highly enriched (about 95%) to guarantee a high neutron flux. After about 50 days the fuel element has mostly burnt up and is exchanged with a new one. In order to cool the neutrons down to only a few neV a couple of steps are needed. The neutrons released in the process of nuclear fission have a very high kinetic energy, which makes any other fission process unlikely since the neutrons simply travel through the nucleus without much interaction. For this reason the fuel cell is located in a pool filled with Deuterium oxide (D_2O, also known as heavy water) at about 300 K, which has about the same mass as neutrons. Via elastic scattering the neutrons transfer their momentum to the D_2O atoms and are thus slowed down from some MeV to about 25 meV. This is followed by a pool filled with liquid Deuterium at a temperature of about 20 K, which slows the neutrons further down to about 2 meV. Afterwards the neutrons are led through a vertically installed neutron guiding tube to a turbine wheel as shown in Figure 1.1. Because of the parabolical shape of the guiding tube faster neutrons are not able to follow the bent and are thus absorbed by it. Furthermore, the height gradient decreases the neutron's kinetic energy while increasing its potential energy. Through collision with the turbine the neutron's kinetic energy is Doppler-shifted below 300 neV. The UCNs are then distributed to four different experiments, namely MAMBO, UCN, EDM and TES. The qBOUNCE experiment is located at the UCN beamline.

Neutrons are considered ultracold when they are totally reflected under any angle of incidence. Because of their relatively low velocity (in the order of several m/s) and subsequently a low kinetic energy, the Fermi potential of the atoms in the coating of every material represent an infinite potential barrier for the neutrons, which they cannot penetrate and are thus totally reflected. Because of this characteristic property it is possible to produce gravitational bound neutron states above the material on which the neutrons bounce. The first proposal for these bound neutron states was in 1978 by Lushchikov and Frank [8]. Experimental proof was given in the year 2002 by Valery Neszvizhevsky [9], see also [10]. In this experiment the transmission of UCNs was measured with varying distance between the absorber-mirror configuration, in Figure 1.2 referred to as Absorber height. The results are shown in Figure 1.2. A clear deviation from the classical expectation is visible, thereby validating the existence of gravitational bound neutron states.
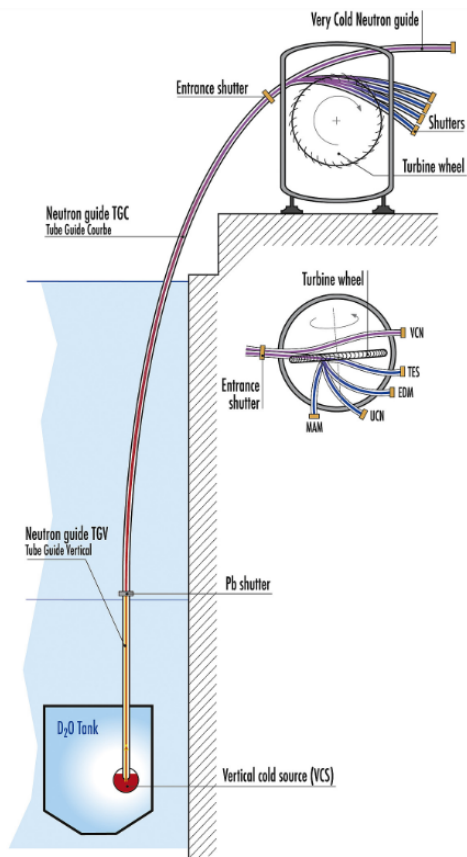
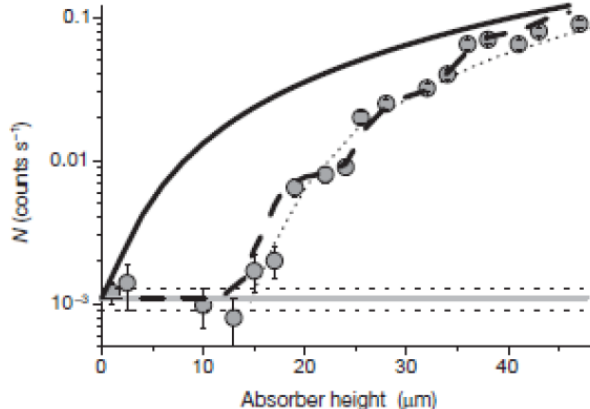Figure 1.1: Schematic drawing of the creation of UCNs at the ILL.[11]

Figure 1.2: Obtained data for an absorber-mirror configuration. The transmission was measured with varying distance between the absorber and mirror, denoted as absorber height. The full line represents the expected classical transmission while the dots represent the actual outcome. This validates the existence of gravitational bound neutron states. Source: [**9**]
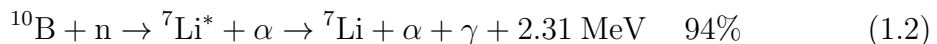
Table 1.1: Classification of neutrons depending on their energy. Values taken from [**12**].

	Fission Neutrons	Thermal Neutrons	Cold Neutrons	UCNs
Energy	2 MeV	25 meV	3 meV	< 100 neV
Temperature	10^{10} K	300 K	40 K	$\backsim 1$ mK
Velocity	10^7 m/s	2200 m/s	800 m/s	$\backsim 5$ m/s
Wavelength	$\backsim 40$ fm	0.18 nm	0.5 nm	$\backsim 80$ nm

Building on these results, the qBOUNCE group at the Atominstitut of the TU Wien tries to obtain a deeper understanding of these gravitational bound neutron states by using Ramsey's method of separated oscillating fields. An important feature of these bound states is that the neutron's eigenenergies are not equidistant, which allows for treating this as a two-level system. The Rasmey setup consists of 5 regions, as shown in Figure 2.3. The neutrons are coming from the left hand side and enter the configuration through Region I, the state selector. This part consists of a plane mirror with an absorber on top at a distance of about 22 μm. The absorber is also a plane mirror but with a roughened surface, which results

in neutrons with a too high eigenenergy getting scattered out of the system when bouncing off of this surface. After this region only neutrons in the lowest states up to a certain cutoff energy can pass the absorber. Regions II and IV are identical and consist of just a plane mirror where the neutrons are propagating freely. With piezo elements these regions can oscillate, thus exciting the neutrons into a higher energy eigenstate. By oscillating with the transition frequency a so called $\pi/2$ flip is induced, which creates a coherent superposition of the states $|p\rangle$ and $|q\rangle$. This coherent superposition is propagating freely in region III, which consists of another plane but slightly longer mirror. The last region, region V, is identical to region I and acts as an analyzer, letting only neutrons in the ground state $|p\rangle$ pass.

Profound knowledge of the state occupation distribution after the absorbers plays an essential role when investigating gravitational bound neutron states. This knowledge is obtained by measuring the height-distribution of the neutrons with a CR39 detector. This detector has a spatial resolution of about 2 μm [13]. The detector consists of an allyl diglycol carbonate, short CR39, coated with a thin ^{10}B layer, as shown in Figure 1.3. The incident neutron reacts in the boron layer and creates both an alpha particle and Lithium nucleus, as shown in Equations 1.2 and 1.3.

$$^{10}\text{B} + \text{n} \rightarrow {}^{7}\text{Li}^* + \alpha \rightarrow {}^{7}\text{Li} + \alpha + \gamma + 2.31\,\text{MeV} \quad 94\% \tag{1.2}$$

$$^{10}\text{B} + \text{n} \rightarrow {}^{7}\text{Li} + \alpha + 2.79\,\text{MeV} \quad 6\% \tag{1.3}$$

Since the alpha particle and the Lithium nucleus are emitted in opposite directions, at least one particle then penetrates the CR39 layer, leaving small craters in the detector material. With an etching processes using sulfuric (H_2SO_4) acid the boron layer gets removed. By immersing the CR39 detector in NaOH (sodium hydroxide) for 5 hours the craters are deepened, creating holes which can be detected with a digital microscope. In order to neutralize the NaOH residuals, the detector is immersed in hydrochloric acid (HCL). The time of the etching process depends on the detector material as well as the temperature of the NaOH bath and takes about 5 hours. The results of longer etching will be shown in great detail in chapter 4.1.
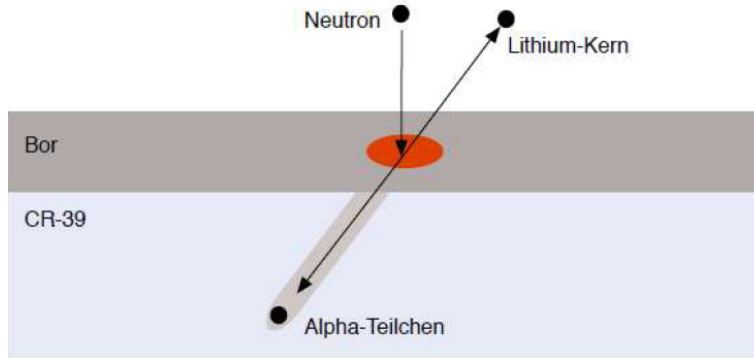
Figure 1.3: Schematic drawing of the boron-CR39 detector. The incident neutron reacts in the boron layer and creates an alpha particle and a Lithium nucelus as shown in Equation 1.2 and 1.3. Source: [**14**]

As already mentioned, the craters in the detector material are scanned with a digital microscope. The x and y coordinates of the craters are extracted and a histogram is created with these neutron coordinates. Afterwards a wavefunction with the first four eigenstates is fitted to this histogram. From this fit the probability distribution of the first three Eigenstates is obtained, as well as an approximation for the absorber height and the energy resolution.

The main focus of this Master thesis lies on systematic tests of the current qBOUNCE setup. These tests include a state occupation measurement using different absorber-mirror configurations with a CR39-coated track detector with a spatial resolution of about 2 μm. With these tests a deeper understanding of the qBOUNCE experiment is obtained.

This thesis is structured as follows: In chapter 2 a theoretical and experimental overview is presented. A short explanation about the differences between Rabi's and Ramsey's method of spectroscopy is given as well as the experimental realization of Ramsey's method of oscillating separating fields within the qBOUNCE experiment.
Chapter 3 explains the measurement process with different absorber-mirror configurations in detail. This is followed by an explanation of the analysis of the CR39 detectors and the process of determining the correct state occupation distribution. Consequently, the measurement results are shown and discussed in section 4.

2 Theoretical Background and Experimental Overview

The qBOUNCE experiment allows high precision spectroscopy of gravitationally bound eigenstates of ultracold Neutrons (UCNs). Since gravitation is significantly weaker than the electromagnetic force at smaller distances, the neutron, because of its (most likely) non existing eletric dipole moment with an upper limit of $|d_{\mathrm{n}}| = -0.21 \pm 1.82 \cdot 10^{-26}$ e $\cdot$ cm [15] is the perfect candidate for this type of experiment. Electric fields from the experimental environment do not have to be accounted for because of the neutron's low electric polarizability and the probably zero charge. Solely magnetic fields have to be taken into consideration due to the neutron's non vanishing magnetic moment, though they can be shielded to a satisfactory level with the implementation of Mu-Metal, which surrounds the entire experiment.

2.1 Obtaining the first eigenenergies of the system

In this chapter an outline is given on how to obtain the eigenenergies of the bound neutrons. For an in-depth description the reader is referred to [16]. The UCN-mirror system can quantum-mechanically be described as a harmonic oscillator with not-equidistant eigenenergies in earth's linear gravity potential. In order to obtain the eigenenergies the time dependent Schrödinger equation (TDSE)

$$\hat{H}(\vec{r},t)\Psi(\vec{r},t) = i\hbar\frac{\partial}{\partial t}\Psi(\vec{x},t) \tag{2.1}$$

has to be solved. The Hamilton operator is of the following form:

$$\hat{H} = -\frac{\hbar^2}{2m}\frac{\partial^2}{\partial z^2} + mgz\Theta(z) + V_0\Theta(-z), \tag{2.2}$$

where z denotes the height of the neutron, m its mass and V_0 the Fermi potential of the mirror. This linear partial differential equation (PDE) is solved by the two

linear independent Airy-functions $\text{Ai}(z)$ and $\text{Bi}(z)$. The most general ansatz to solve this PDE is a linear combination of the two Airy-functions

$$\psi(z) = c_1 \cdot \text{Ai}\left(\frac{z}{z_0} - \frac{E}{E_0}\right) + c_2 \cdot \text{Bi}\left(\frac{z}{z_0} - \frac{E}{E_0}\right), \tag{2.3}$$

where

$$z_0 = \sqrt[3]{\frac{\hbar^2}{2m^2 g}} \approx 5.87\,\mu\text{m} \quad \text{and} \quad E_0 = mgz_0 \approx 6.02 \cdot 10^{-13}\text{eV} \tag{2.4}$$

By calculating the roots of the Airy-functions the eigenenergies are obtained. Since the Airy-functions are transcendent in nature the roots have to be numerically computed. The first 4 eigenenergies of the bound neutron states are listed in Table 2.1 and plotted in Figure 2.1.

Table 2.1: Calculated energies of the first 4 Eigenstates and the respective height obtained from $E_n = mgz_n$.

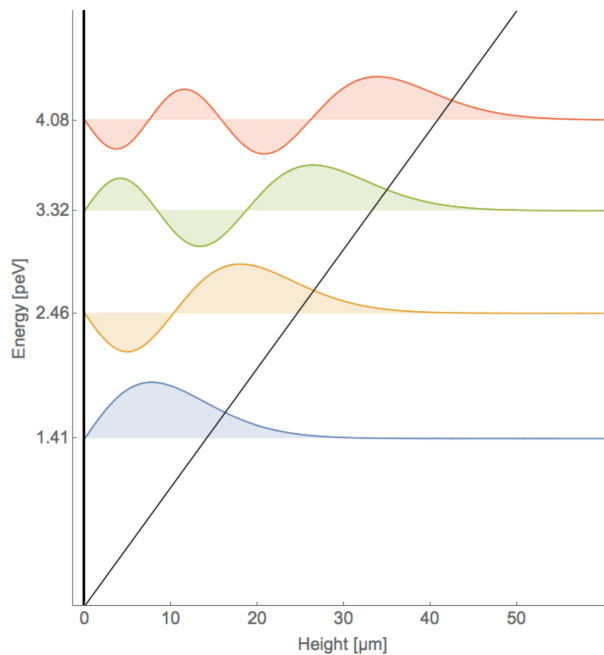| Eigenstate	E_n [peV]	z_n [μm]
$\lvert 1 \rangle$	1.41	13.75
$\lvert 2 \rangle$	2.46	24.04
$\lvert 3 \rangle$	3.32	32.47
$\lvert 4 \rangle$	4.08	39.92

Figure 2.1: Plot of the first 4 Eigenstates of the Airy-function with the respective energy. The eigenenergies are not equidistant, neither are the transition frequencies. This is the important reason why this system can be treated as a two level system. Source: [17].

2.2 Rabi Spectroscopy

This method of spectroscopy was firstly introduced by Isidor Isaac Rabi in the year 1938 [18] and was awarded the Nobel Prize in 1944. The first realization of Rabi Spectroscopy in the context of gravitational bound states was realized within the dissertation of Tobias Jenke [19] and further optimized by Gunther Cronenberg [20]. This setup basically consists of 3 separate regions as shown in Figure 2.2. Region I is a combination of a flat mirror and a roughened scatterer at a distance of approximately 22 µm on top of the mirror. When UCNs enter the first region those with high energy (in Figure 2.2 denoted as $|q\rangle$) are scattered out of the system by the roughened scatterer on top, meaning that only neutrons with the lowest eigenenergies can propagate through (neutrons in the state $|p\rangle$). Ideally only neutrons in the ground state $|1\rangle$ pass this region, although in reality the first three eigenstates have a non vanishing probability of passing through. The selected neutrons are then propagating freely in Region II. Region II consists of only a flat mirror which is mechanically vibrating, thus exciting the neutrons to a

higher energy state. The vibration frequency was calculated beforehand in order to guarantee a π flip, meaning they are now in the higher energy state $|q\rangle$. The first five transmission frequencies are shown in table 2.2. When looking at this system as a two state system (as is done in Figure 2.2) all neutrons are now in the $|q\rangle$ state. The last region, Region III, consists of the same mirror-scatterer combination, which means only neutrons in the ground state $|p\rangle$ are passing through. In the ideal case the transmission after Region III drops to zero since all neutrons are in the excited state $|q\rangle$.

For a quantum mechanical description one has to solve the time dependent Schrödinger equation with the following Hamiltonian:

$$\hat{H} = \begin{pmatrix} \frac{\hbar\omega_{pq}}{2} & \frac{1}{2}\hbar\Omega_R \mathrm{e}^{-\mathrm{i}\omega t} \\ \frac{1}{2}\hbar\Omega_R \mathrm{e}^{+\mathrm{i}\omega t} & \frac{-\hbar\omega_{pq}}{2} \end{pmatrix}. \tag{2.5}$$

Here, $\omega_{pq} = (E_q - E_p)/\hbar$ denotes the frequency difference between the two states and ω the frequency of the driving field. Ω_R is called Rabi frequency which is the state oscillation frequency between $|p\rangle$ and $|q\rangle$. The probability for being found in an excited state can be written as a function of time:

$$P(t) = \left(\frac{\Omega_R}{\Omega_R'}\right)^2 \sin^2\left(\frac{\Omega_R'}{2}t\right), \tag{2.6}$$

with the effective Rabi frequency:

$$\Omega_R' = \sqrt{\Omega_R^2 + (\omega_{pq} - \omega)^2} = \sqrt{\Omega_R^2 + \delta^2}, \tag{2.7}$$

where δ represents the detuning from resonance. This means that the state occupation probability is oscillating with half of the effective Rabi frequency. For a more detailed description the reader is referred to [21] or [22].

Theoretically, when vibrating at resonance the transmission drops to zero since all neutrons, now in the excited state $|q\rangle$, are scattered out of the system in region III. In reality the following factors make a transmission drop to zero impossible:

- The state selection in Region I is not ideal. Typical values of state occupation are 40-60% $|1\rangle$, 30-50% $|2\rangle$ and 0-15% $|3\rangle$. The state occupation measured within this master thesis will be explained in greater detail in chapter 4.

- Exact resonance exists only for one velocity. The undefined velocity distribution from the UCNs results in a smearing out effect.
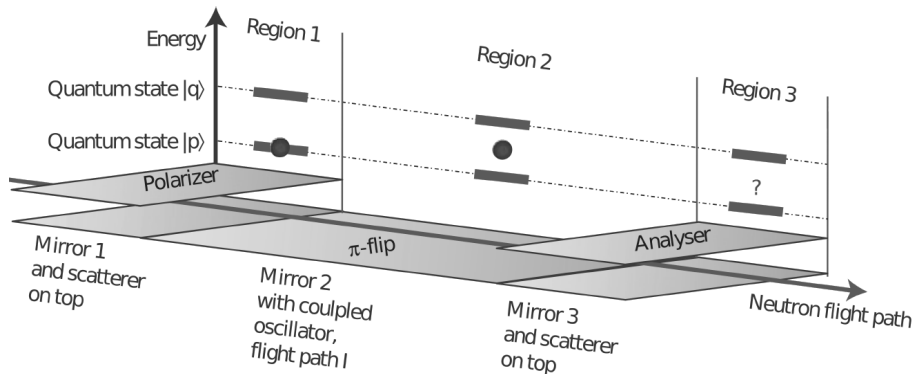
Figure 2.2: Schematic drawing of the Rabi setup. Region I is used for state preper-
ation, in region II the neutron can propagate freely and region III is
again a state selector identical to region I. [20]

Table 2.2: Calculated transition frequencies ω_{pq} in [Hz] for the first five eigenstates.

Eigenstate	$|1\rangle$	$|2\rangle$	$|3\rangle$	$|4\rangle$	$|5\rangle$
$|1\rangle$	0	254.54	462.93	647.10	815.46
$|2\rangle$		0	208.39	392.57	560.93
$|3\rangle$			0	184.18	352.54
$|4\rangle$				0	168.36
$|5\rangle$					0

2.3 Ramsey Spectroscopy

Ramsey's method of separated oscillating fields is the extension of Rabi's method.
It was firstly introduced in 1950 and also awarded with the Nobel Prize in 1989.
The method is explained in great detail in [23]. Instead of one π-flip two sepa-
rate $\pi/2$-flips are made as shown in Figure 2.3. With this method the frequency
resolution can be further optimized. A comparison of the transition plot between
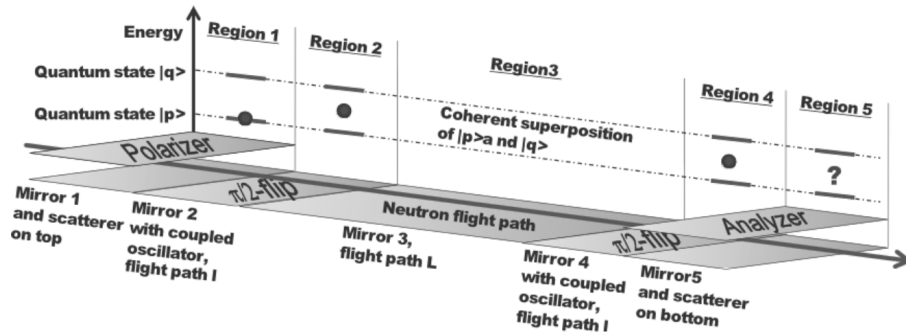Rabi's and Ramsey's method of oscillating fields is shown in Figure 2.4.

Figure 2.3: Schematic drawing of the Ramsey setup. Region I is acting as a polarizer, meaning that only neutrons in the groundstate $|p\rangle$ are propagating through, higher energy states are scattered out of the system. Region II and IV are identical and induce a $\pi/2$ flip. In region III the neutrons propagate freely in a coherent superposition of $|p\rangle$ and $|q\rangle$. Region V is acting as an analyzer, meaning that only neutrons in the groundstate $|p\rangle$ pass through. **[24]**

Region I is called a polarizer. In this region the ground state $|p\rangle$ is selected. It is identical to Region I in the Rabi setup and consists of a flat mirror with a roughened scatterer at a distance of about 22 μm. Ideally only neutrons in the ground state $|p\rangle$ pass this region.

Region II consists of solely a flat mirror which is mechanically vibrating via piezo elements. The mirror is vibrating at half the amplitude in the Rabi setup in order to induce a $\pi/2$-flip instead of a full π-flip.

Region III consists of a long mirror at which the neutron can propagate freely. For a perfect state preparation the neutron is now in the coherent superposition

$$|\Psi\rangle = \frac{1}{\sqrt{2}}(|p\rangle + \mathrm{i}\,|q\rangle). \tag{2.8}$$

At this point the crucial aspect of Ramsey's method of separated oscillating fields becomes apparent: Because of the undefined velocity distribution of the neutrons coming from the beam tube, the time spent at region III differs for every neutron. Neutrons with fitting velocity entering region IV will be at exact resonance with the second $\pi/2$-flip. The state vector is again at its starting position, thus completing the cycle with a whole π-flip. On the other hand, the state vector of neutrons with ill fitting velocity is pointing 180° in the other direction, thus the second $\pi/2$-flip will rotate the state vector back to the ground state $|p\rangle$.

Region IV is identical to Region II, inducing another $\pi/2$-flip on the neutrons. Neutrons with the right velocity are entering this region at exact resonance and

will be excited to the $|q\rangle$ state. UCNs at off-resonance will return to the ground state $|p\rangle$.

Region V is identical to region I and acts as an analyzer, letting only neutrons in the ground state $|p\rangle$ pass. After region V a proportional counter is measuring the energy of the transmitted neutrons.

When Ramsey's method of separated oscillating fields is applied to neutrons with a distinct velocity distribution, the peaks next to the main peak are getting suppressed. With this a higher frequency resolution can be obtained as shown in Figure 2.4.
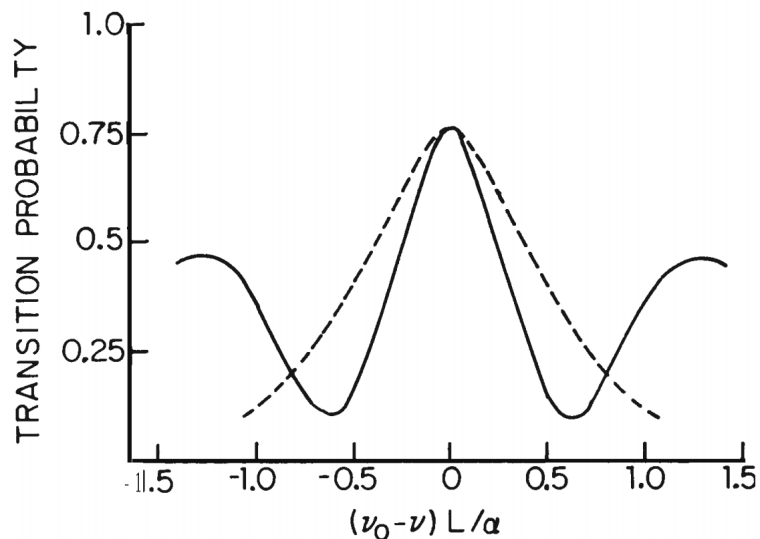
Figure 2.4: Transistion probability as a function of frequency when the particles have a Maxwellian velocity distribution. L being the distance between oscillating field regions, α the most probable velocity and ν is the oscillation frequency $\omega/2\pi$. The dashed line represents the transistion probability for Rabi spectrocopy and the full line for Ramsey spectroscopy respectively. [25]

2.4 Current setup for state occupation measurements

As already explained earlier, the focus in this master thesis lies on systematic tests of the state occupation for different absorber-mirror configurations. In Figure 2.5 a schematic drawing of the setup used to determine the state occupation is shown. The entire experiment is located on a massive granite stone which can be

levelled horizontally at 3 points. The neutrons are entering the setup through the beam line on the left, where the velocity of the neutrons can be selected with an aperture. In the course of this master thesis the selected velocity was in the range of 5 - 13 m/s. The neutrons then enter the absorber-mirror configuration, where the approximate distance between absorber and mirror was measured with linear gauges to be around 22 μm. At the end a CR39 detector with a spatial resolution of about 2 μm ([7]) is located. The UCNs create defects in the detector material. These defects can later on be further analyzed with a digital microscope, where the x and y coordinates of each neutron are extracted. In short, a histogram is created out of the neutron events. By fitting this histogram with the wavefunctions of the first four eigenstates the state occupation distribution can be calculated. This paints a clear picture of what happens after each region of Ramsey's setup and gives a deeper understanding of the entire experiment.
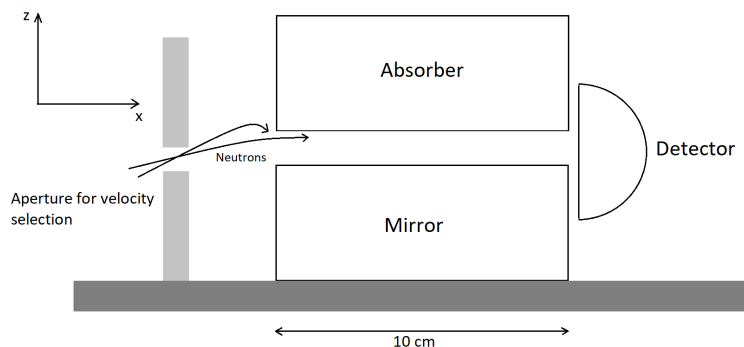
Figure 2.5: Schematic drawing of the setup used to determine the state occupation for different absorber-mirror configurations. The slit height between Absorber and mirror is about 22 μm, thereby letting only neutrons in the first 4 eigenstates travel through.

It is desired to only let neutrons in the first eigenstate pass through region I, which would show as a clear transmission drop. But, as already explained in Section 2.2, several limitations make a transmission drop to 0 impossible. By knowing the probabilities of higher eigenstates passing through region I, one can anticipate and interpret the result more correctly. The obtained results are shown in section 4.

3 Explanation of the read-out process

In the following section an explanation of the chemical procedure as well as how to obtain the probability amplitude of region I and V is given. The data readout was done using Mathematica scripts written by Hanno Filter, Martin Thalhammer and Tobias Jenke. The data readout processes are explained in sections 3.2 to 3.5.

3.1 Chemical procedure

The composition and working principle of the CR39 neutron detectors is explained in great detail in section 1. In order to make a read out possible the following steps are needed:

1. The boron layer, which acts as a neutron converter, has to be removed. This can be achieved by using 20% H_2SO_4 + H_2O_2.

2. The defects created by either the Lithium core or the α-particle are widened and deepened using 20% sodium hydroxide (NaOH). This process makes the defects detectable for an optical microscope. For the entirety of the etching process, the CR39 detectors are placed inside a thermally stable heating bath at a temperature of 42°C for a duration of exactly 5 hours. The effects of over-long etching periods are thoroughly discussed in section 4.1.

3. Afterwards, by immersing the CR39 detector into hydrochloric acid (HCl), the NaOH gets effectively neutralized, thus stopping the etching process.

After these steps the coating material should have dissolved and the neutron defects are deepened enough to continue with the next step, which is scanning the neutron tracks with a digital microscope.

3.2 Scanning with the digital microscope *Olympus BX41*

The digital microscope "Olympus BX41" was used to scan the different CR39 detectors. It is placed on a separate table in order to minimize vibrations. The CR39 detectors are placed under a lens on a movable plate. On top of this lens a camera is mounted. At every step this camera takes a picture with an area of 288.8×216.6 μm^2, which corresponds to 1376×1032 pixel [26]. The plate is able to move in all three spacial directions and can be controlled either via a script or manually with a joystick. The microscope is operated using a software called "CellˆD". The magnification of the microscope used was 50x. Before the readout process starts a couple of steps are needed to optimally configure the microscope:

1. The camera has to be aligned in parallel to the plate on which the detectors are placed. In order to do so, a configuration sample is used on which several dots and a cross are drawn. To start the process the center of this cross has to be found by moving the plate with the joystick. When moving, for example, to the left corner of the cross, followed by moving to the right corner, the line should always be inside the frame without having to adjust the up and down direction. This is achieved by loosening the screw on the camera and manually rotating it to achieve a precise alignment. At the end the screw is tightened and the next configuration processes can start.

2. On top of the microscope plate a micrometer screw and three positioning screws are located. These screws are used to align the neutron track with the movement of the plate in the y direction. This guarantees that the entirety of the neutron track does not drift outside of the pictures during the scanning process. Since every neutron track has a slightly different bending, this has to be done for every detector separately. The easiest way to do this is to find the beginning of the neutron track (lets say on the left hand side of the detector) and, using the joystick, move to the other end of the neutron track (the right hand side). Depending on how far off the neutron track on the other end is, one has to use these screws to move the neutron track back into the picture. By repeating this process iteratively one obtains a better and better alignment from the neutron track with the moving microscope plate. The goal is that the entire neutron track is always visible when moving the plate from the left hand side to the right hand side without altering the x direction of the plate.

3. The range of the moving table has to be configured. In order to do one has to open the CellˆD software and click on the following buttons (the software is

operated in German, which is why the commands are also german): "Extras" → "Einstellungen" → "Tisch" → "Tischebereich". The z range has to be manually configured by turning the joystick knob left and right (moving the table up and down respectively). This sets the upper and lower limit of the z range of the table. The x and y ranges are configured automatically.

4. In order to remove the impurities on the lens as well as dust in the light path, following steps are needed: The camera should not be in live mode. There should be no sample on the microscope table. Afterwards, click "Aufnahme" → "Referenzbild aufnehmen" → "Durchlicht" and just click "weiter" until the popped up window disappears. When returning to live mode the picture should be free of most impurities, if not repeat the step until the result is satisfying.

When these steps are finished one has to define an automation script. This script automatically controls the microscope plate and alters the y direction in order to scan the entire CR39 detector. Solely the z direction (i.e. the focus) has to be controlled manually for each of the 460 pictures. Click "Aufnahme" → "Tisch" → "Tisch-Manager". By doing so a red crosshair appears. Now, using the joystick, one has to manually find the y-center of the neutron track and click on the button which reads "Zentrum setzen". In the same window one can change the number of x and y steps (Zeilen and Spalten). At the end one has to save this automation script under a fitting name, for example "460x1_Detector_ID". For the read out of the CR39 detectors within this master thesis the steps in the y direction (Zeilen) was set to 460 and the steps in the x direction (Spalten) was set to 1. A schematic picture of the automation script is shown in Figure 3.1.
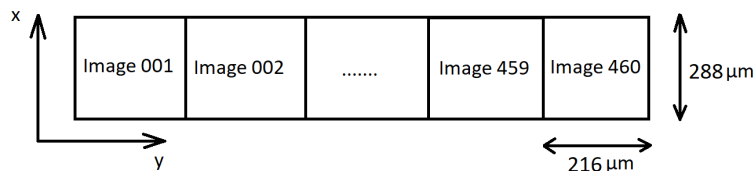

Figure 3.1: Schematic drawing of the automation script used for scanning the CR39 detectors in this master thesis.

The script can now be started by clicking on "Automatisierung Definieren". Now one has to select the just defined automation script as well as a directory into which the pictures are saved. Afterwards one can click "Automatisierung starten" and the microscope plate should move to the starting point. At each step the z-direction, responsible for the focus, has to be altered manually by turning the joystick knob left or right, moving the table up or down respectively.

3.3 Extracting the coordinates of the neutrons

This section will give a qualitative explanation on how to use the script "Junction.nb" to extract the neutron coordinates from the 460 picutres obtained from section 3.2. An example of such a picture is shown in Figure 3.2. For a more detailed explanation the reader is referred to [26].
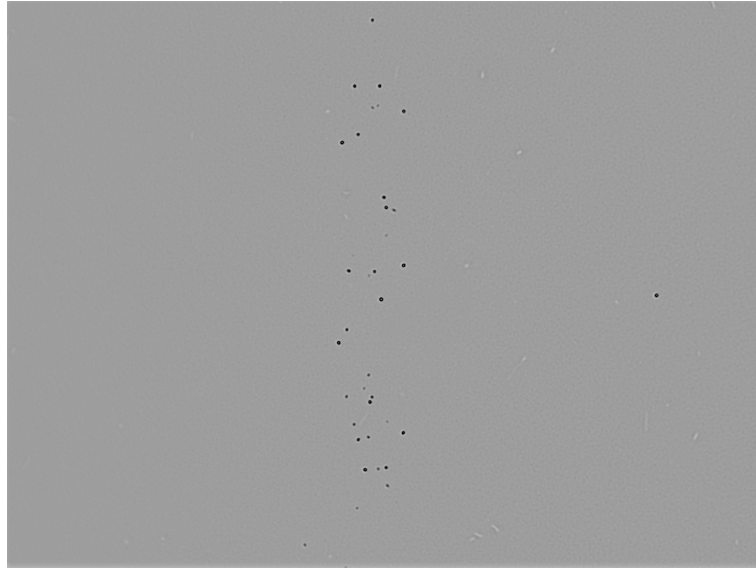

Figure 3.2: Example of one picture of a neutron track. This is one picture of the detector with the ID 003 which will be discussed later in this thesis.

This Mathematica script to further analyze the pictures and extract the respective coordinates is written by Hanno Filter. The most recent library used here is called "CR39 Analysis" with the version number 1.10.5. The structure of the script is explained below, where the bold text is the name of the respective headline in the Mathematica script:

1. **Normalise Images**: Here the row and column length as well as the scan geometry - for example horizontal or vertical meander - is defined. These attributes have been defined in section 3.2 in the automation script and should here be entered accordingly. In the next step each of the 460 pictures is normalized to a standardized colour. In this step the colour of each image is set to a same background.

2. **Detection via Front-End** In this step each picture can be viewed separately. Under the point "Detection Control" a threshold can be set which

alters the background. The background goes darker while the detected neu-
tron points can be seen as white spots. This tool is an important feature
which helps to check the parameters after which a neutron is detected. An
example for a good and ill fitting threshold value is shown in Figure 3.3.

3. **Detection via Automation Script** Here the parameters are set after which
a neutron is detected. The "BinParameter" is set differently for every one of
the four CR39 detectors evaluated in this master thesis. This is the threshold
parameter explained in the step above. How to set the other parameters like
"AreaParameter" or "ElongationParameter" can also be checked in the step
"Detection via Front-End". As explained in [**26**] at page 151: "After image
capture and normalization the next step is the determination of the position
of nuclear tracks. Therefore, a threshold for the intensity value range is
defined, which selects all pixels over that threshold and determines the size
of clusters of the selected pixel." These selected pixels are then converted to
μm (i.e. x and y coordinates) for further analysis. After this step a .track file
is generated which contains the extracted x and y coordinates of the detected
neutrons, as well as other parameters like area and elongation.

(a) An example case if the threshold value is taken too high.

(b) An example case for a fitting threshold value.
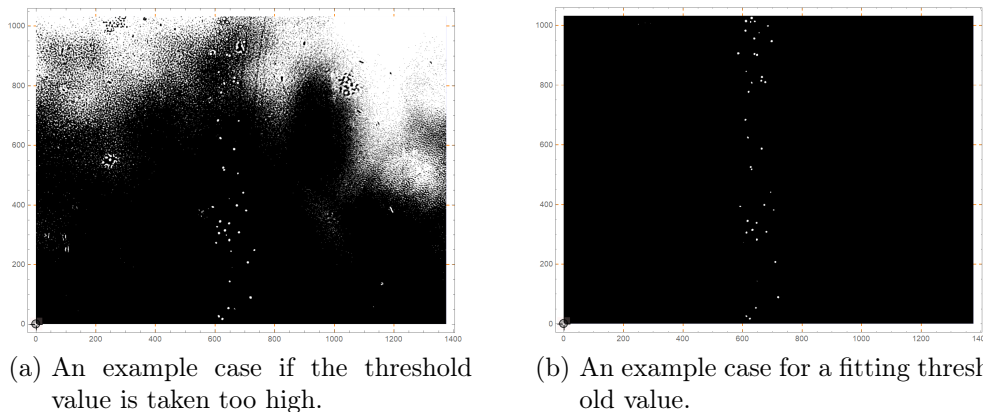
Figure 3.3: Two example cases for different threshold values.

4. **Show Results** In this step a plot of the scanned region is created. Such
plots are shown for example in Figures 4.1 to 4.3 where the scan geometry
was a 5x5 horizontal meander.

5. **Machine Learning** This is the last but most important feature of this
script. Here the track file is further analyzed by a machine learning algo-
rithm trained on hand selected neutron events. The previously created track

file is read in. This algorithm divides the detected neutron events into different classes. Depending on the angle of incidence, regularity and other attributes following classifications are defined: "Neutron Point", "Neutron Extreme", "Neutron Faint", "Neutron Double", "Neutron Triplet", "Neutron Inclined", "Candidate Faint", "Candidate Extreme", "Systematic Unclear", "Systematic Crack", "Systematic Dust ", "Artefact Noise" "Artefact Small Image". The algorithm is trained on hand-selected neutron events. Those events were classified manually by Hanno Filter in order to train the Mathematica script. Some example cases of the training data are shown in Figure 3.4. The detection probability of each event can be weighed by a constant number. For example if one expects a lot of neutrons classified as "Systematic Dust", the weight should be in the range of 1. By optimizing these parameters one is able to assure a good quality of the classification results. At the end, by clicking on "Save Data" another file of the type `.selected` is generated which again contains the x and y coordinates but also another attribute called "Class", which defines the classification result.
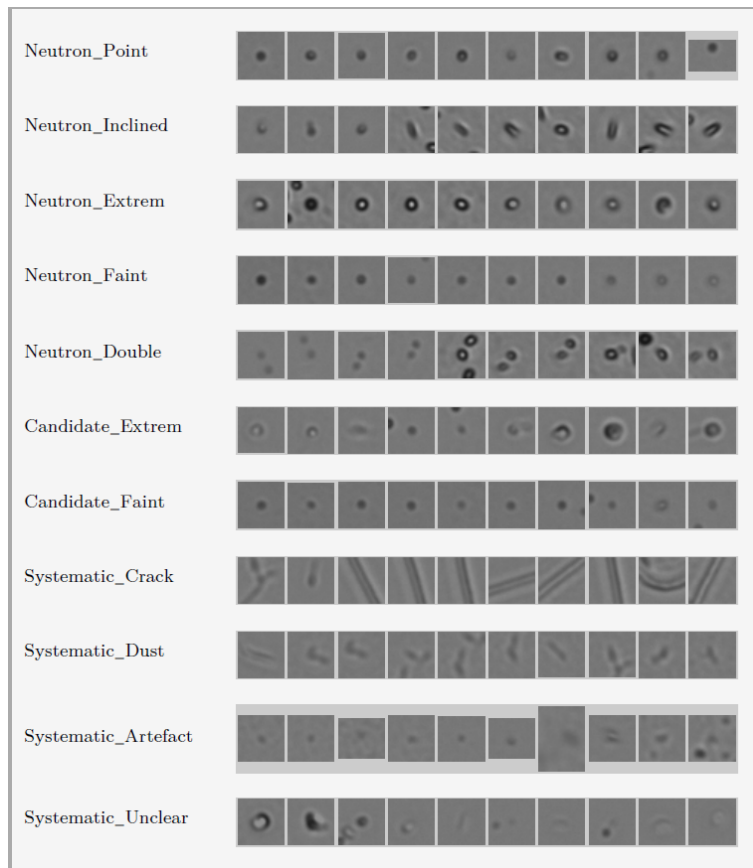
Figure 3.4: Manually classified neutron track candidates used to train the machine
learning algorithm. Source: [**26**]

This is the last step of the Mathematica script "Junction.nb". An explanation
on how to unbend the neutron track is given in section 3.4.

3.4 Unbending the neutron track

In this section an explanation is given on how to use the Mathematica script "Date-
naufbereiten Entbiegen" in order to straighten the neutron track. This script is
written by Tobias Jenke and the key functionalities were explained to me verbally.
For a more detailed description on how the script operates, the reader is referred
to [**25**] pp. 32 ff. The basis builds the `.selected` file which was created at step 5
in Section 3.3. Each headline will be discussed separately and is written in bold
letters.

1. **Evaluation ID** Here the `.selected` file, which was created in Section 3.3 under point 5, is read in and a plot of the raw data is created, as shown for example in Figure 4.13. By selecting only neutron classes which fit the shape of the neutron track and excluding such that are most likely impurities, systematic errors are reduced and the wavefunction fit yields more significant results. These results are thoroughly discussed in section 4.3.3.

2. **Rotate the data** In this step a linear model fit is done and every neutron coordinate is rotated by the degree of its gradient. This will assure a horizontal neutron track.

3. **BendingCorrection** This is the most important step of this script. At first, a histogram of the neutron track is created. Important parameters in this step are `zlb` and `zub`, which define the lower and upper z boundary. The lower boundary can be set to start well below the neutron track (if the edge of the neutron track starts at 100 μm then `zlb` can be defined as for example 70 μm). The value for the upper boundary should be taken at the maximum of the histogram. `bins` defines the bin size, which is in the order of 0.5 - 1 μm. Afterwards a non linear model fit is created.

   This step is followed by a spline interpolation. One example of such a spline interpolation is shown in Figure 3.5. As one can see the neutron track is divided into 5 parts of equal length, were each part is fitted separately with an error function. Subsequently, a straight line is fitted onto this spline interpolation as a mean to measure the gradient of the neutron track. Afterwards every z coordinate is subtracted by its corresponding interpolation coordinate, thus levelling them on an even ground. An example for the final fit is shown in Figure 3.6, where the neutron track has already been straightened. Afterwards a .txt file with the histogram data and a plot for the straigth neutron track are created, as shown for example in Figures 4.19 and 4.20.
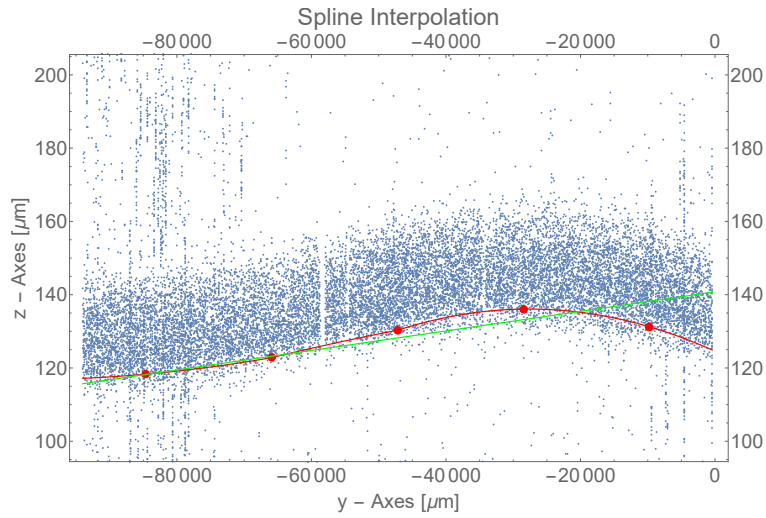
Figure 3.5: A plot for one of the three possible spline interpolation schemes which can be used to create a straight neutron track. The green line represents the tilt in z direction of the neutron track, the red line is the corresponding spline interpolation. The coordinates for every neutron point are subtracted by the corresponding value of the spline interpolation.
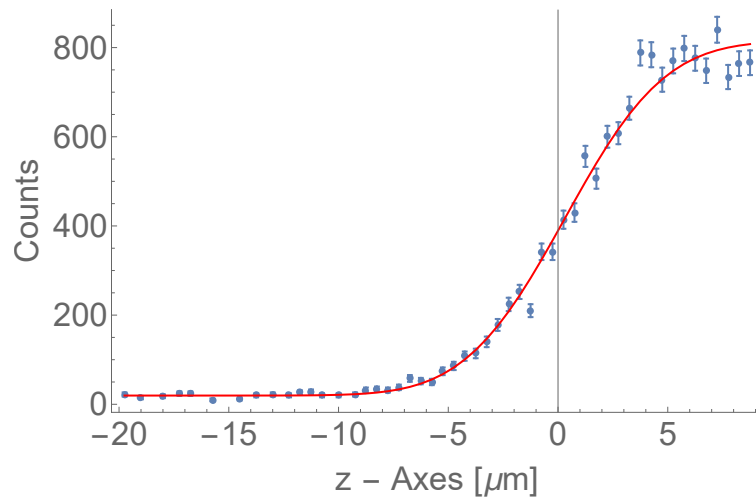

Figure 3.6: An example plot for the final error function fit. The error function is drawn as the red line, the blue dots represent the histogram of the neutron track.

3.5 Obtaining the state occupation probabilities

In this last step the created histogram is fitted with two Airy functions in order to obtain the state occupation results. The script is called "WF Fit" and was written by Tobias Jenke and Martin Thalhammer[1]. The name of the headline in the Mathematica script is, once again, written in bold letters.

1. **Map Preparation** Here the parameters are defined which are necessary for the wavefunction fit. `tnom` defines the number of Eigenstates to fit. In this master thesis the first four Eigenstates were fitted. The fit-function consists of an incoherent sum of the individually populated states $\varphi_n(z, t_1)$ at measurement time t_1, as explained in [**25**] on page 47:

$$|\psi(z, t_1)|^2 = N \sum_n |C_n(t1)| \left(|\varphi_n(z - z_0)|^2 * f(z, \sigma) \right) + N_0. \qquad (3.1)$$

   Here, N corresponds to the normalization factor, $C_n(t1)$ are the respective occupation parameters, z_0 is the offset in z direction, $f(z, \sigma)$ is a Gaussian function with the spatial resolution σ and N_0 corresponds to the background.

   For the parameters `tmapc02qua`, `tmapc03qua` and `tmapc04qua`, which are used in the Mathematica script, one has to define an interval. This sets the range in which the occupation parameters are fitted. It is important to note that the first Eigenstate is taken to be 1 and all probabilities are not normalized at this point. When fitting a histogram for the first time the best way to start is with both large intervals and step-sizes. There are several fits necessary in order to find the optimal result. At each fit the interval should be reduced while simultaneously decreasing the step-size. `tmapl` defines the absorber height in μm, `tmapzshift` the offset in the z direction between fit and histogram and `tmapsigma` the spatial resolution (which equals the standard deviation of the fit) in μm.

   When the fit routine starts it simultaneously fits the first value of the defined interval for every parameter and calculates the corresponding chi squared. This is done for the entire interval. The result with the smallest chi squared is then taken to be the best fitting value. Since this Mathematica script was initially written for the Quantum Bouncing Ball (QBB, which is explained for example in [**Cronenberg, 2015**]), and in the QBB experiment there

---

[1]Unfortunately at the moment of writing this master thesis, Martin Thalhammer has not yet finished writing his doctoral thesis in which a theoretical description of the wavefunction fit would be given. I was, however, in direct communication with Martin Thalhammer and he thoroughly explained to me how how one should use the Mathematica script. For an in-depth description the reader is referred to the doctoral thesis of Martin Thalhammer.

are always 2 regions (first an absorber-mirror, then a small step followed by another mirror), this script expresses the first 20 Eigenstates from region 2 in the basis of the 4 Eigenstates in region 1. The function `ij` then calculates the overlap probability of those Eigenstates. Since, in this master thesis, there is only the first absorber-mirror region, the overlap probability is not vanishing only for the first 4 Eigenstates (since there is no step, thus no need to evolve the Eigenstates).

2. **Show Map** In this step a plot of the fit result and the chi squared of each parameter is presented together with all results of the fitting parameters. Once again the values for the Eigenstates are not normalized and the first Eigenstate is taken to be 1. After normalizing these results one ends up with the final outcomes, shown for example in Table 4.4.

Another important parameter is the so called "Verträglichkeit", which is the reduced chi squared, also called Goodness of the fit. This value should at least be above 5%, although its importance should not be overrated. For example: if a wavefunction fit is done using a histogram with fewer neutrons (in the order of 3000 or lower), then the corresponding error bars of the histogram are larger. This leads to the case that one can fit this histogram with almost anything, increasing the Goodness of the fit. Still, this parameter can be used to determine the accuracy of the fit nonetheless.

When these steps are finished the data read out process is complete and one can start thinking about the implications of each result.

4 Measurements and Evaluation

4.1 Results of longer etching times

This section gives a qualitative explanation on the dependency of detected neutrons with regards to the etching time. The process is explained in Section 3.1. Since the CR39 detector had to be taken out of the microscope for each etching process, a cross was carved into the material in order to find the same spot on the microscope again and make a comparable and reproducible analysis possible. For longer etching times it is evident that more neutrons are detected. At a certain etching time, however, the neutron points begin to merge, resulting in a quality-decrease of the following neutron point classification. Two different detectors were evaluated and the results are shown in the sections below. Both detectors were exposed to the neutron beam for a duration of 190 s and had the same chemical treatment. The only difference between these detectors is the CR39 plastic. The raw data of detected neutrons are shown in Figures 4.1 to 4.9. The obtained data from the machine learning script are shown in Table 4.1 and 4.2.

4.1.1 Detector ID 103
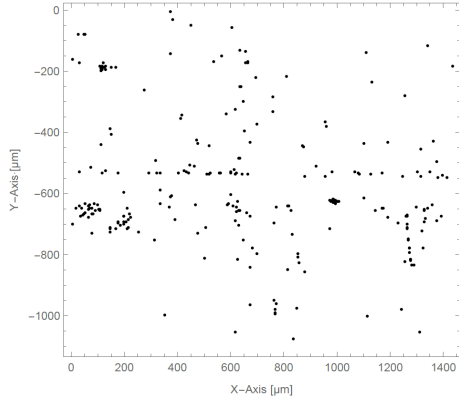
(a) Detected neutrons after an etching time of 2.5 hours. 234 neutrons were detected in total.
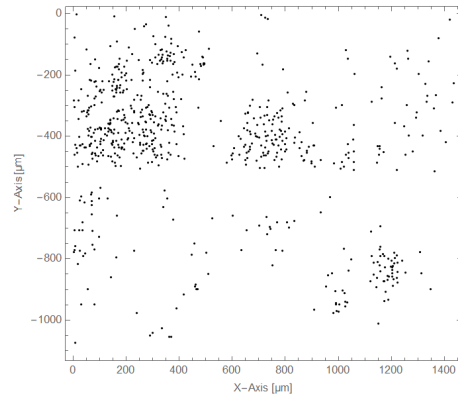
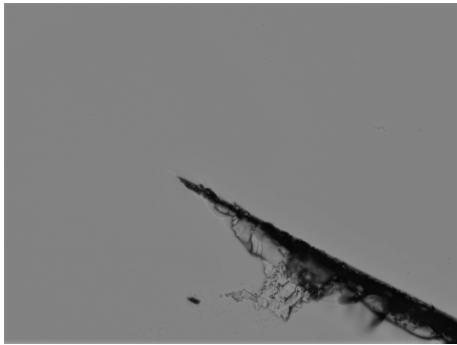(b) Detected neutrons after an etching time of 4 hours. 662 neutrons were detected in total.

Figure 4.1: Raw data plot of the detected neutrons.
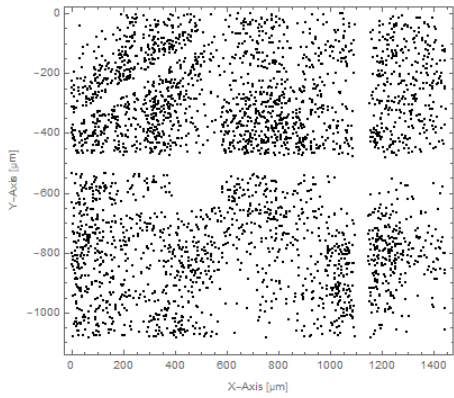
(a) Detected neutrons after an etching time of 5.5 hours. 3335 neutrons were detected in total.
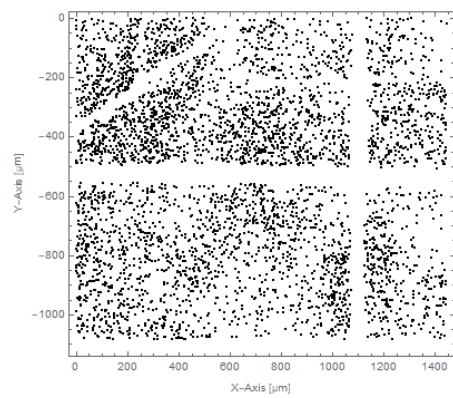
(b) Detected neutrons after an etching time of 6 hours. 4142 neutrons were detected in total.

Figure 4.2: Raw data plot of the detected neutrons.
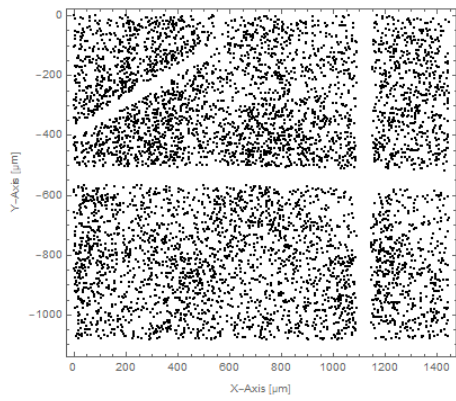
(a) Detected neutrons after an etching time of 7.5 hours. 5193 neutrons were detected in total.
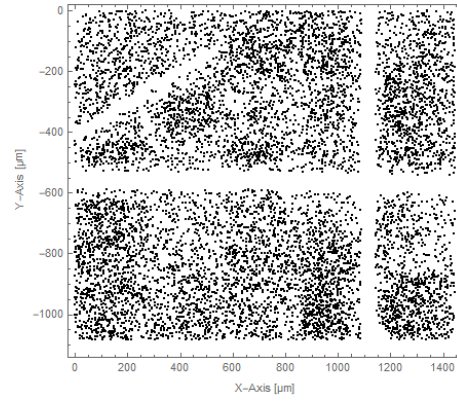
(b) Detected neutrons after an etching time of 12 hours. 7897 neutrons were detected in total.

Figure 4.3: Raw data plot of the detected neutrons.

Table 4.1: Obtained number of classifications from the machine learning script for varying etching times.

Etching time in hours	2.5	4	5.5	6	7.5	12
Neutron Point	0	0	23	110	449	1
Neutron Double	4	1	3	16	178	1853
Neutron Triplet	0	0	0	0	0	0
Neutron Inclined	15	1	5	16	301	59
Neutron Faint	5	23	486	600	228	0
Neutron Extreme	0	0	0	0	0	0
Candidate Faint	90	590	2156	2077	1190	46
Candidate Extreme	111	35	646	1299	2827	4973
Artefact Noise	0	4	0	6	2	2
Artefact Small Image	0	0	0	0	0	0
Systematic Crack	0	0	0	0	0	0
Systematic Dust	9	0	9	19	18	963
Systematic Unclear	0	8	0	0	0	0
Total number of Neutrons	234	662	3335	4142	5193	7897

Looking at Table 4.1, the following observations can be made: An increase in total neutron numbers is clearly visible. At a certain point, after 6 hours of etching, one can see a decrease in both Candidate Faint and Neutron Faint, while Neutron Point and Candidate Extreme increases. This is most likely due to the fact that the neutron points become broadened and deepened with longer etching time. The neutrons classified as "faint" are more fittingly classified as Neutron Point and Candidate Extreme respectively. After an etching time of 12 hours the classification for Neutron Point drops to 1, while categorizing about 10 times more neutrons as Neutron Double compared to the 7.5 hours of etching. Overall the number of neutrons classified as Neutron Double increases over time, indicating the merging of neutron points for over-long etching periods.

Regarding the etching time of the CR39 detectors for state occupation measurements an etching time of 5 hours was chosen. Below example pictures for each time step are shown.
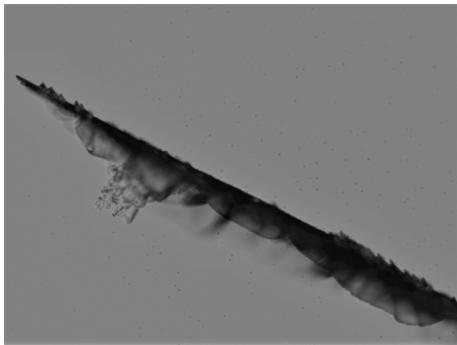
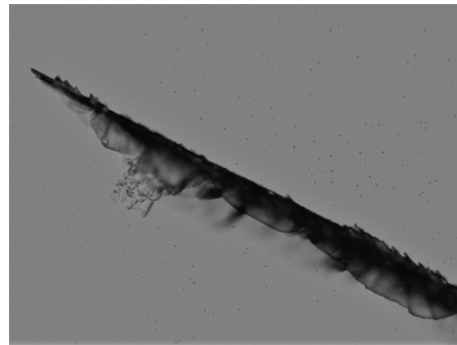(a) Detected neutrons after an etching time of 2.5 hours.

(b) Detected neutrons after an etching time of 4 hours.

Figure 4.4: Example picture in order to compare the different etching times.
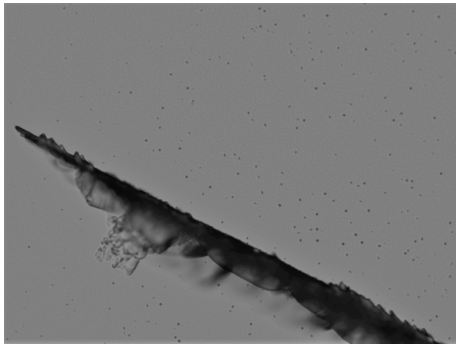

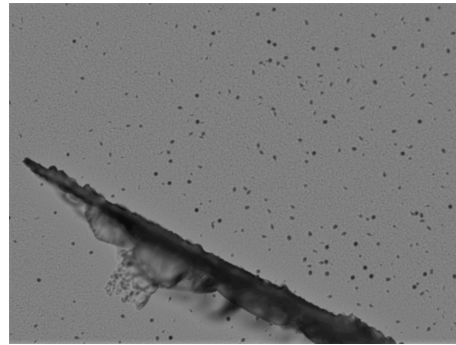(a) Detected neutrons after an etching time of 5.5 hours.

(b) Detected neutrons after an etching time of 6 hours.

Figure 4.5: Example picture in order to compare the different etching times.

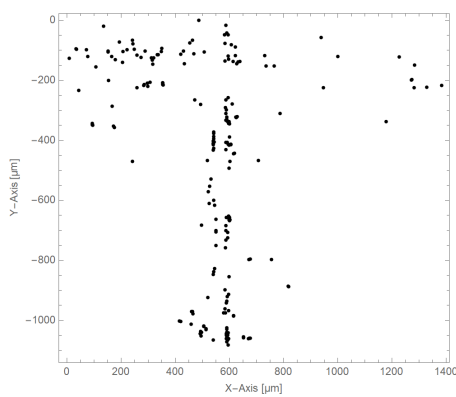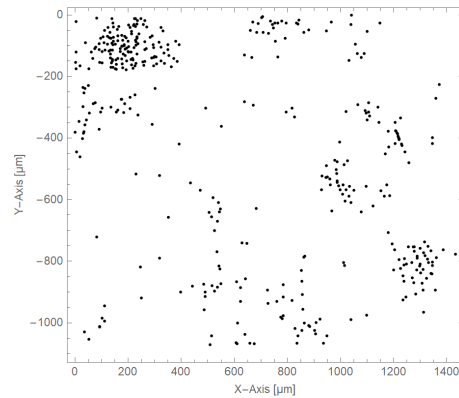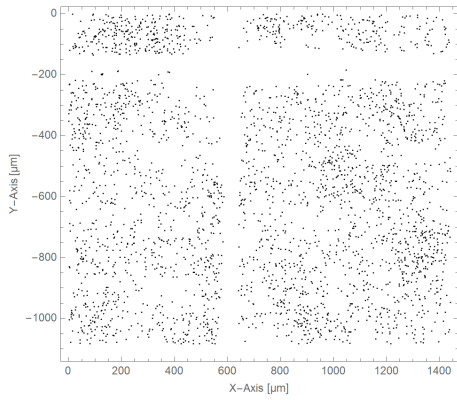(a) Detected neutrons after an etching time of 7.5 hours.

(b) Detected neutrons after an etching time of 12 hours.

Figure 4.6: Example picture in order to compare the different etching times.

4.1.2 Detector ID E03

The obtained plots for varying etching time for Detector E03 are shown below.

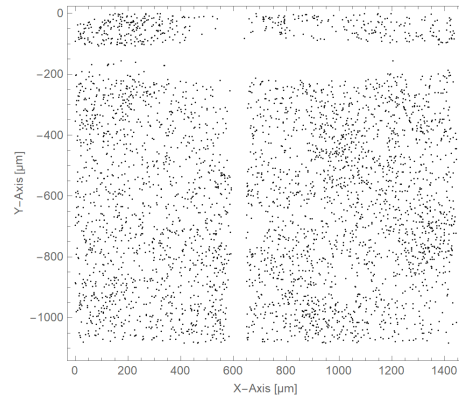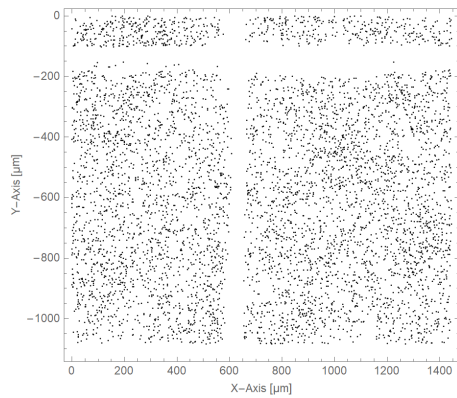(a) Detected neutrons after an etching time of 2.5 hours. 210 neutrons were detected in total.

(b) Detected neutrons after an etching time of 4 hours. 405 neutrons were detected in total.

Figure 4.7: Raw data plot of the detected neutrons.

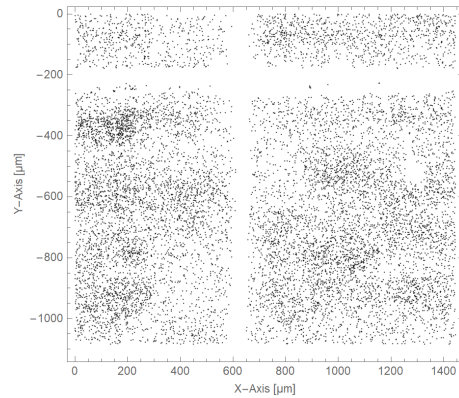(a) Detected neutrons after an etching time of 5.5 hours. 2494 neutrons were detected in total.

(b) Detected neutrons after an etching time of 6 hours. 2985 neutrons were detected in total.

Figure 4.8: Raw data plot of the detected neutrons.

(a) Detected neutrons after an etching time of 7.5 hours. 4495 neutrons were detected in total.

(b) Detected neutrons after an etching time of 12 hours. 7897 neutrons were detected in total.

Figure 4.9: Raw data plot of the detected neutrons.

Table 4.2: Obtained number of classifications from the machine learning script for varying etching times.

Etching time in hours	2.5	4	5.5	6	7.5	12
Neutron Point	0	2	34	82	74	0
Neutron Double	73	7	60	250	1793	5076
Neutron Triplet	0	0	0	0	0	0
Neutron Inclined	12	8	4	17	81	1
Neutron Faint	0	76	177	95	6	0
Neutron Extreme	0	0	0	0	0	0
Candidate Faint	0	220	548	304	52	0
Candidate Extreme	125	89	1665	2234	2445	4845
Artefact Noise	0	1	7	0	0	0
Artefact Small Image	0	0	0	0	0	0
Systematic Crack	0	0	0	0	0	0
Systematic Dust	0	2	6	3	44	531
Systematic Unclear	0	0	0	0	0	0
Total number of Neutrons	210	405	2501	2985	4495	10452

It is clear to see that the total number of neutrons increases, as expected. From 6 to 7.5 and 7.5 to 12 hours a significant increase in the neutrons classified as "Neutron Double" is visible, which indicates again the merging of two neutron points. Since this detector had a lot of impurities (i.e. scratches), the results are not as satisfying as before with Detector 103. Nevertheless, it paints a clear picture of what happens after each time interval.

4.2 Estimating the neutron-beam divergence

Another systematic test which was done during the beam-time was investigating the divergence of the neutron-beam between the beam-line and the aperture for velocity selection. This was done by attaching one CR39 detector directly behind the beam-line and another one in front of the velocity selector. A schematic drawing is shown in Figure 4.12. Both detectors are of equal length and are mounted approximately on the same height. For each CR39 detector a histogram with a

binning of 500 μm in z range is created, which is shown in Figures 4.10 and 4.11. The first and last z coordinate with more than 100 counts is defined as the edge of the neutron track. A broadening of the histogram is clearly visible.
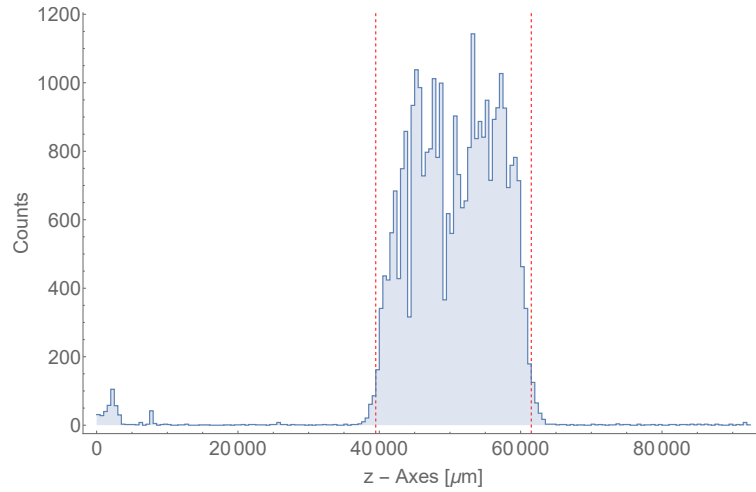

Figure 4.10: Histogram created for the CR39 detector T35 directly behind the beam-line. The lower value is 39500 μm and the upper value is 61500 μm. The bin size was 500 μm.
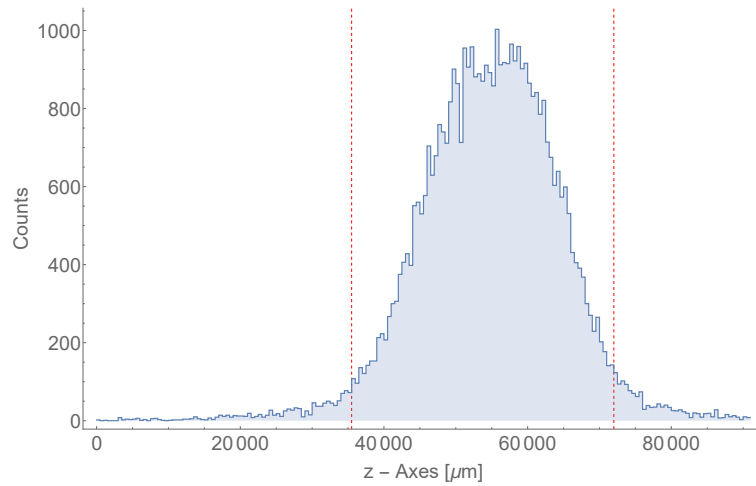
Figure 4.11: Histogram created for the CR39 detector 016 in front of the aperture for velocity selection. The lower value is 35500 μm and the upper value is 72000 μm. The bin size was 500 μm.
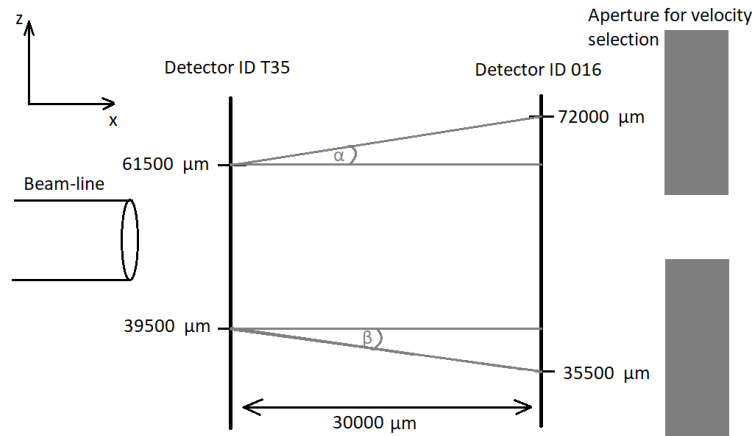
Figure 4.12: Schematic drawing of the setup used to investigate the neutron-beam divergence. The neutrons enter the setup from the left hand side through the beam-line, where the first detector is mounted. In front of the velocity selector another detector is mounted. By defining the edge of the neutron-beam as the bin in z direction with more than 100 neutron counts, the beam divergence between these edges can be approximated.

Table 4.3: Obtained values from the histogram. "Edge start point" and "Edge end point" represent the first and last bin in z direction with more than 100 neutron counts. The bin size was 500 μm.

	Total neutron counts	Edge start point [μm]	Edge end point [μm]
ID T35	32391	39500	61500
ID 016	44533	35500	72000

By doing simple arithmetics one can approximate the degree of divergence of the neutron-beam, as is done in Equation 4.1 and 4.2 below:

$$\tan(\alpha) = \frac{72000 - 61500}{30000} \quad \rightarrow \quad \alpha = \arctan\left(\frac{72000 - 61500}{30000}\right) = 19.29° \quad (4.1)$$

$$\tan(\beta) = \frac{39500 - 35500}{30000} \quad \rightarrow \quad \beta = \arctan\left(\frac{39500 - 35500}{30000}\right) = 7.60° \quad (4.2)$$

Where α is the degree of divergence for the top part and β the degree of divergence for the bottom part of the beam-line. One should keep in mind that this is a simple approximation. In reality the detectors were not mounted on exactly the same height. There was about 1 mm difference. Nonetheless the results paint a good picture of the divergence of the neutron-beam.

4.3 Region I, Detector ID 003

As already explained in section 3.1 a crucial point for Rabi and Ramsey spectroscopy is the knowledge of the state occupation. The data discussed in this section was obtained using the setup shown in Figure 2.5. The raw data, meaning all detected neutrons without any alteration, is shown in Figure 4.13. A clear bending of the neutron track is visible, as well as several impurities (the horizontal lines, which are made up of individually detected points), most likely originating from the imperfect coating of the CR39 detector. It is apparent that some data has to be cut away in order to obtain a satisfying result for the state occupation distribution.
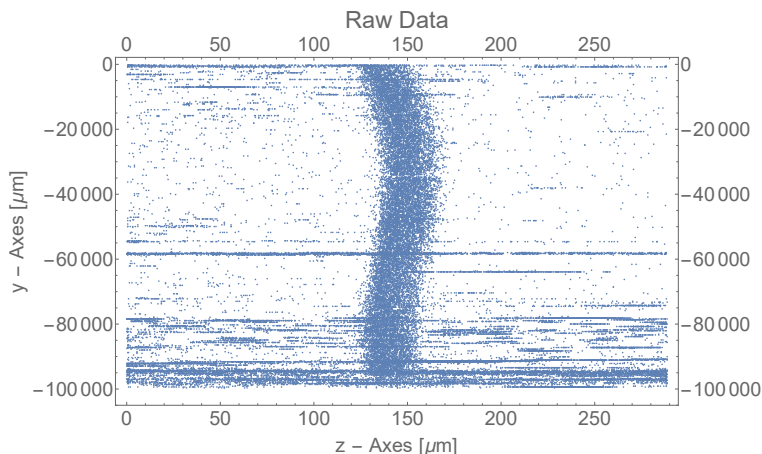

Figure 4.13: Raw data of the detected neutrons without any alteration. 40537 neutrons were detected in total.

Using the machine learning script one is able to get rid off most, but not all impurities. The machine learning script detects the impurities (which are Figures 4.14 to 4.16 show the classification results with more than 100 neutron counts.
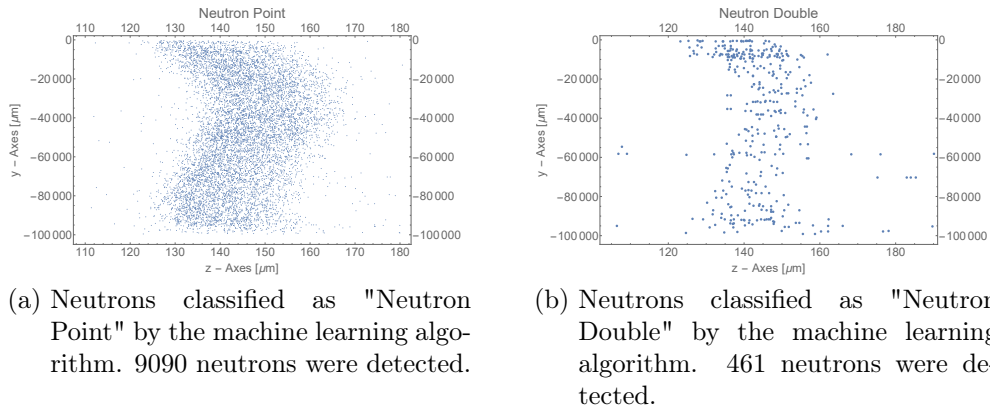
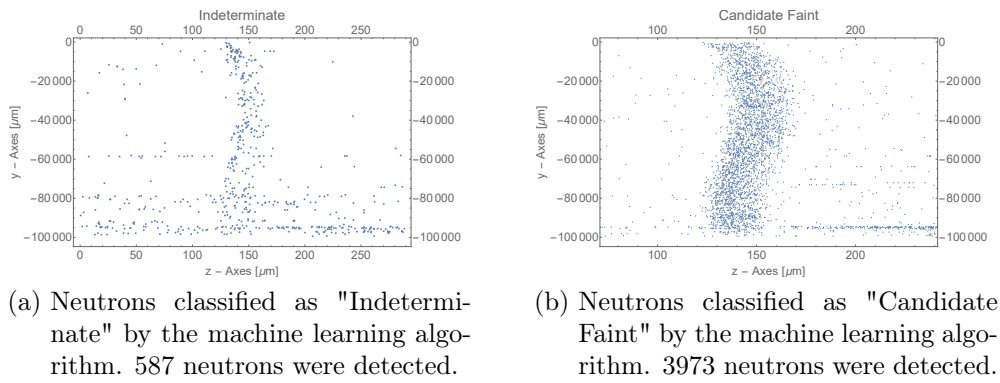(a) Neutrons classified as "Neutron Point" by the machine learning algorithm. 9090 neutrons were detected.

(b) Neutrons classified as "Neutron Double" by the machine learning algorithm. 461 neutrons were detected.

Figure 4.14: Detected and classified neutrons by the machine learning algorithm.

(a) Neutrons classified as "Indeterminate" by the machine learning algorithm. 587 neutrons were detected.

(b) Neutrons classified as "Candidate Faint" by the machine learning algorithm. 3973 neutrons were detected.

Figure 4.15: Detected and classified neutrons by the machine learning algorithm.

(a) Neutrons classified as "Candidate Extreme" by the machine learning algorithm. 15826 neutrons were detected.

(b) Neutrons classified as "Systematic Dust" by the machine learning algorithm. 10231 neutrons were detected.
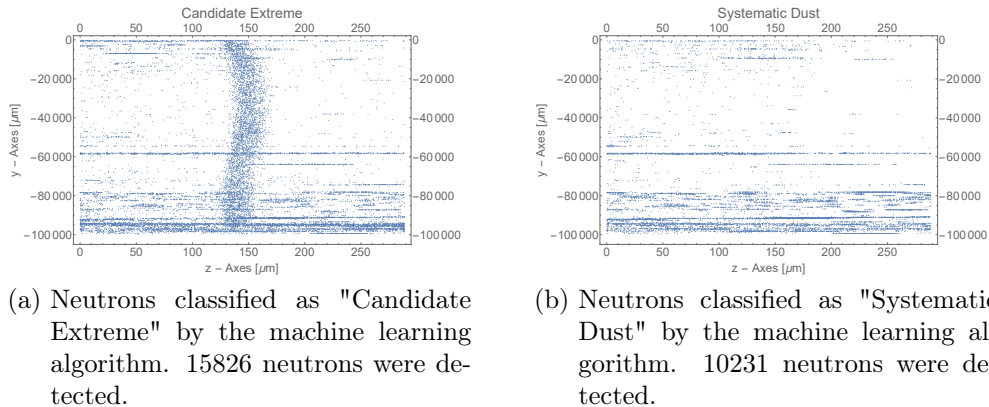
Figure 4.16: Detected and classified neutrons by the machine learning algorithm.

In order to control the legitimacy of the state occupation results, three different approaches have been carried out:

1. All classification events (except those classified as "Systematic Dust") were taken into account. The result is shown in Figure 4.17. The total amount of neutrons is 29937. This is the approach of most statistical importance. The downside, however, is apparent when looking at the left side of Figure 4.17. A lot of impurities are visible. This is a direct consequence of including neutrons classified as "Candidate Extreme" from Figure 4.16 a.

2. All classification events were taken into account. The neutron track was divided into 10 parts of equal length and each part was fitted separately with the wavefunctions. The weighted mean for each result was then calculated with the weight being the standard deviation of the first error function fit, as explained in Section 3.4 under point 3. The idea behind this step is to reduce the statistical influence of regions in which the result was obviously blurred by some effect. Section 4.3.2 shows that the results are very much the same for both the full and the divided neutron track respectively. This confirms that even for neutron tracks with a high bending the results are not drastically different.

3. Neutrons classified as "Candidate Extreme" were excluded, resulting in a neutron track which is almost free from impurities, although only containing 14111 neutrons. This could be a great problem for statistics, since the total amount of neutrons is cut in half. Section 4.3.3 shows that the impact of fewer neutrons for the results of the state occupation is extremely small and can thus be neglected.

4.3.1 Approach 1: All neutrons are taken into account

It is clear to see that the neutrons classified as Systematic Dust can be excluded without losing information or impactful statistics. The remaining neutrons as shown in Figure 4.17 were taken for the following evaluation.
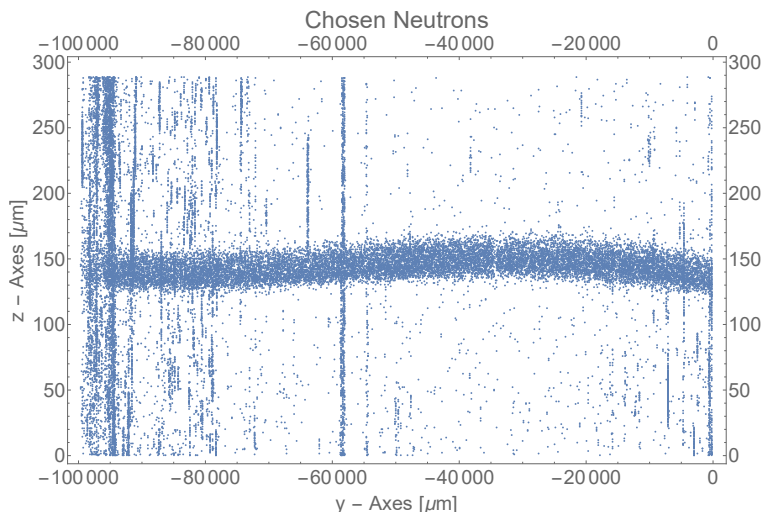

Figure 4.17: A plot of all chosen neutrons: Neutron Point, Neutron Double, Indeterminate, candidate Faint and candidate Extreme. The neutrons classified as Systematic Dust have been excluded. The remaining neutrons are 29937 in total.

In order to guarantee the straightness of the neutron track, all points together have been fitted with a straight line and the gradient of this line was calculated. Subsequently all neutron points are rotated clockwise by the degree of the gradient in order to make it more parallel to the y - Axis.
Some impurities are still remaining and clearly visible. Since they are all located on the left and some on the right hand side of the detector, the intervall was chosen to range from -94000 μm to -400 μm. The straight line at -60000 μm was also cut out and one ends up with the remaining neutrons shown in Figure 4.18.
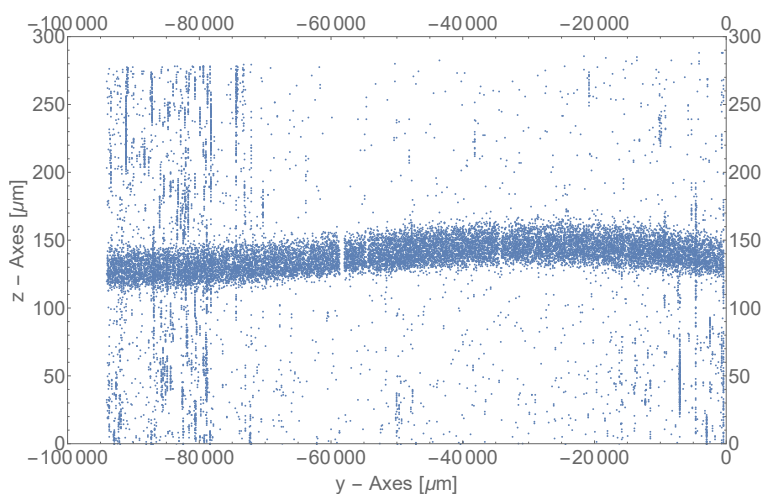
Figure 4.18: A plot of the neutron track after most impurities have been cut out. The remaining neutrons are 21522 in total.

Now an error function is fitted at a histogram of the neutron track followed by a spline interpolation in order to unbend the neutron track, as explained in section 3.4. The z coordinates of the neutrons have also been shifted so that the edge of the neutron track starts at zero. The final neutron track is shown in Figure 4.19.
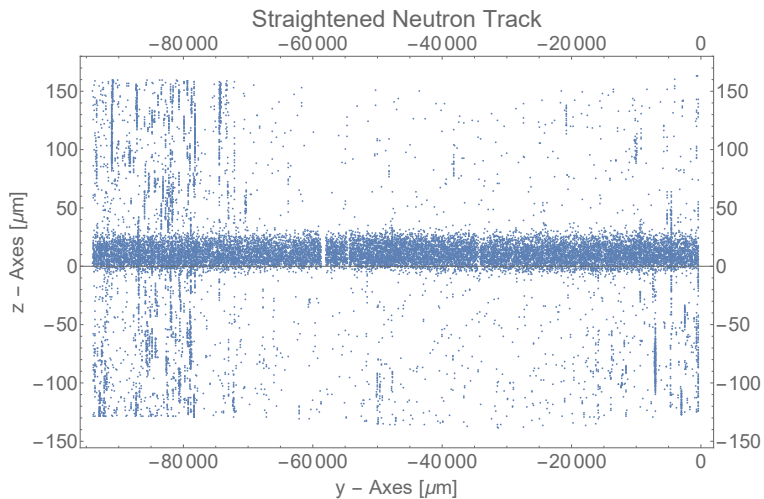

Figure 4.19: A plot of the straightened neutron track. The z coordinates of the neutrons have also been shifted so that the edge of the neutron track starts at zero.

Finally, a histogram is made out of this straightened neutron track. The histogram shown in Figure 4.20 is used for fitting the Airy functions.
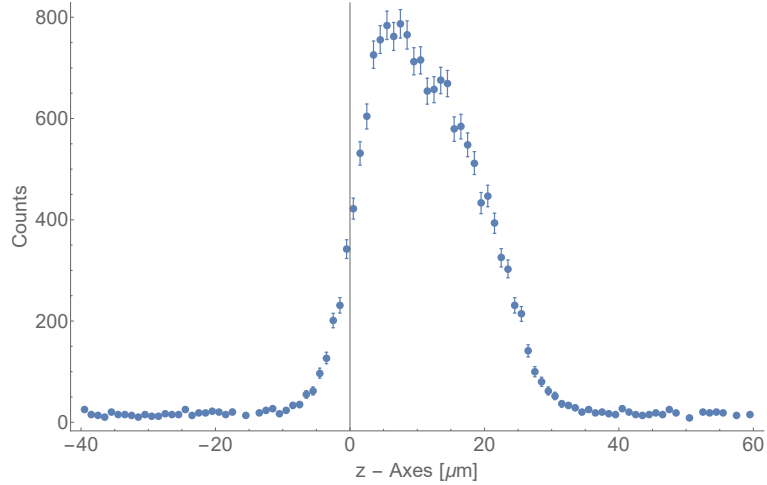

Figure 4.20: A histogram obtained from the straight neutron track shown in Figure 4.19.

The results for fitting the two Airy functions are shown in Table 4.4 and 4.5.

Table 4.4: Obtained values from fitting the histogram containing all 21522 neutrons with the first three eigenstates. Approach 1 for Detector ID 003. The reduced chi squared of this fit is $\chi^2 = 0.93$ with 51 DOF.

$\|C1\|^2$ [%]	$47.1^{+1.5}_{-1.1}$
$\|C2\|^2$ [%]	$40.0^{+2.9}_{-3.7}$
$\|C3\|^2$ [%]	$13.0^{+5.3}_{-3.2}$
Spatial resolution [µm]	$3.66^{+0.11}_{-0.13}$
Absorber height [µm]	$30.58^{+1.38}_{-0.80}$

Table 4.5: Obtained values from fitting the histogram containing all 21522 neutrons with the first four eigenstates. Approach 1 for Detector ID 003. The reduced chi squared of this fit is $\chi^2 = 0.93$ with 50 DOF.

$|C1|^2$ [%]	$45.3^{+4.1}_{-2.7}$
$|C2|^2$ [%]	$37.6^{+3.5}_{-3.5}$
$|C3|^2$ [%]	$12.1^{+4.0}_{-4.0}$
$|C4|^2$ [%]	$5.0^{+5.7}_{-0.3}$
Spatial resolution [µm]	$3.60^{+0.11}_{-0.08}$
Absorber height [µm]	$30.22^{+0.82}_{-1.06}$

When looking at the state occupation shown in Table 4.4 and 4.5, it is apparent that the third Eigenstate is not entirely suppressed, meaning that the state selection in Region I is not working as planned. With the following steps from section 4.3.2 and 4.3.3 an attempt in validating or even improving on the data is made. For the conclusion of these attempts the reader is referred to the end of chapter 4.3.3.

4.3.2 Approach 2: Dividing the neutron track into 10 parts of equal length

The only difference to the approach made in section 4.3.1 lies in the fact that the neutron track shown in Figure 4.19 was divided into 10 parts of equal length, where each part has a length of 9360 µm (since the total neutron track ranges from -94000 to -400 µm totalling 93600 µm). Each part is fitted with an error function in order to obtain the standard deviation of the neutron track (i.e. the spread). A histogram for each part is done separately, resulting in 10 histograms where each histogram has a specific standard deviation σ_i. Finally, each histogram is fitted separately with the wavefunctions in order to obtain the state occupation parameters. These results are then used to calculate the weighted mean $\overline{x}$ for each parameter according to equation 4.3:

$$\overline{x} = \frac{\sum_{i=1}^{10} w_i x_i}{\sum_{i=1}^{10} w_i} \tag{4.3}$$

with $w_i = \frac{1}{\sigma_i^2}$.

The results for each interval with its corresponding standard deviation are shown in Table 4.6 below.

Table 4.6: Standard deviation and state occupation probability for each corresponding interval. The standard deviation was obtained by fitting each interval with an error function. It has to be mentioned that in some cases the error for the coefficients are 0.0, which does not, however, mean that in reality the errors are zero. The errors are calculated from the chi squared parabola. Since in some cases the chi squared parabola is too flat, one would have to take a wide interval for the state occupation fit. This results in a computation time of several days for each interval, which was not feasible during the course of this master thesis and hence not done. This has to be taken into consideration when looking at the final result in Table 4.7.

Interval [µm]	Standard deviation σ_i [µm]	$|C1|^2$ [%]	$|C2|^2$ [%]	$|C3|^2$ [%]
-400 to -9760	3.223	$49.1^{+3.6}_{-3.9}$	$36.9^{+10.1}_{-10.3}$	$14.0^{+18.7}_{-7.9}$
-9760 to -19120	5.668	$55.8^{+19.7}_{-8.4}$	$21.0^{+0.0}_{-14.0}$	$23.2^{+0.0}_{-4.1}$
-19120 to -28480	4.058	$55.4^{+8.2}_{-9.9}$	$44.6^{+8.6}_{-0.0}$	$0.0^{+0.0}_{-0.0}$
-28480 to -37840	3.143	$46.2^{+4.5}_{-4.1}$	$39.7^{+6.0}_{-10.4}$	$14.1^{+1.4}_{-9.6}$
-37840 to -47200	3.526	$38.4^{+5.5}_{-3.9}$	$30.8^{+10.2}_{-9.8}$	$30.7^{+8.9}_{-14.5}$
-47200 to -56560	2.631	$45.2^{+3.8}_{-2.4}$	$46.7^{+3.8}_{-3.9}$	$8.1^{+4.2}_{-2.9}$
-56560 to -65920	2.348	$52.7^{+4.3}_{-3.0}$	$43.0^{+3.7}_{-6.0}$	$4.3^{+3.4}_{-2.8}$
-65920 to -75280	2.644	$50.0^{+2.4}_{-2.8}$	$29.2^{+5.0}_{-5.7}$	$20.7^{+6.1}_{-5.3}$
-75280 to -84640	3.052	$45.5^{+5.1}_{-4.8}$	$36.3^{+6.1}_{-10.0}$	$18.2^{+11.0}_{-1.7}$
-84640 to -94000	2.892	$45.2^{+3.8}_{-4.0}$	$39.6^{+9.2}_{-7.7}$	$15.2^{+16.2}_{-9.3}$

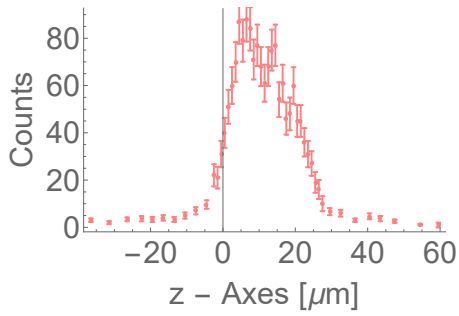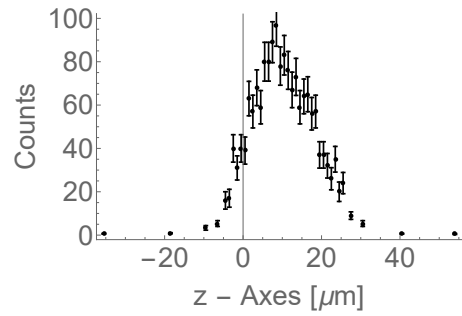A histogram for each interval is shown in Figures 4.21 to 4.25

(a) Obtained histogram for the interval
-400 to -9760 µm.

(b) Obtained histogram for the interval
-9760 to -19120 µm.

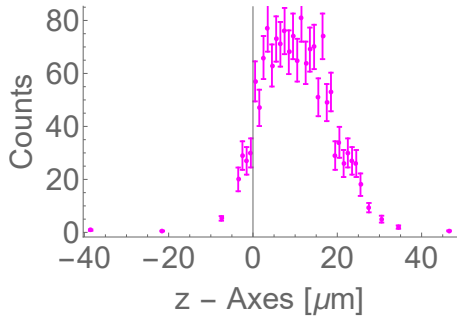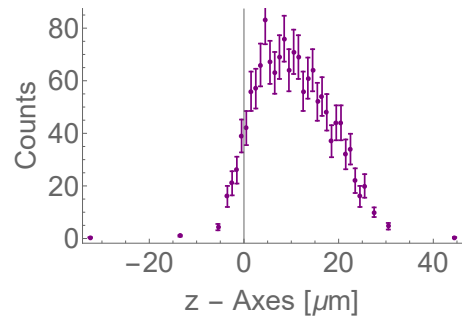Figure 4.21: Obtained histogram for the interval approach

(a) Obtained histogram for the interval
-19120 to -28480 µm.

(b) Obtained histogram for the interval
-28480 to -37840 µm.
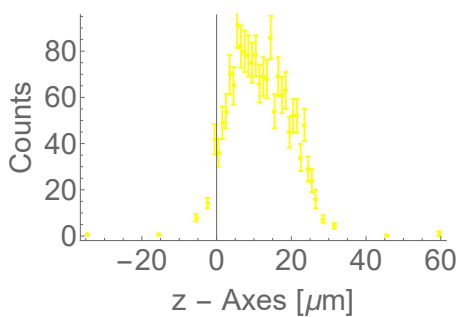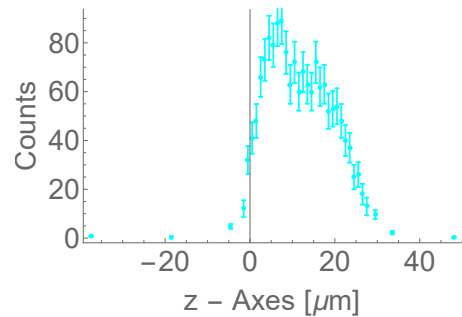
Figure 4.22: Obtained histogram for the interval approach

(a) Obtained histogram for the interval
-37840 to -47200 µm.

(b) Obtained histogram for the interval
-47200 to -56560 µm.
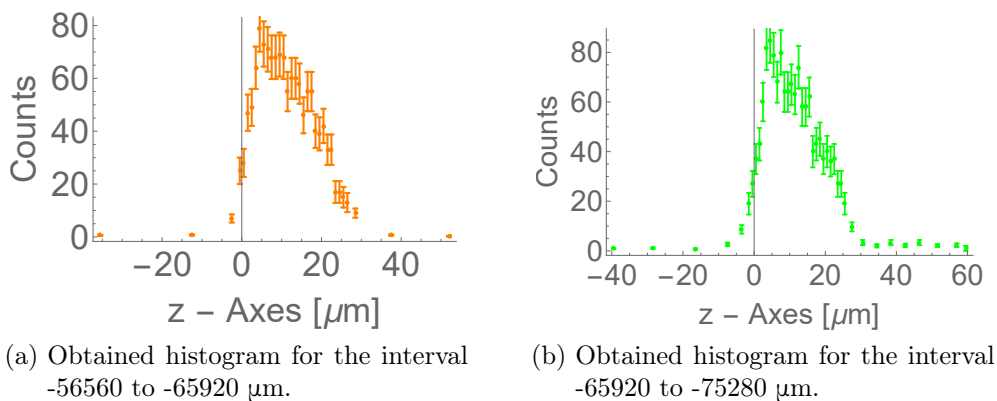
Figure 4.23: Obtained histogram for the interval approach

(a) Obtained histogram for the interval -56560 to -65920 μm.

(b) Obtained histogram for the interval -65920 to -75280 μm.

Figure 4.24: Obtained histogram for the interval approach

(a) Obtained histogram for the interval -75280 to -84640 μm.

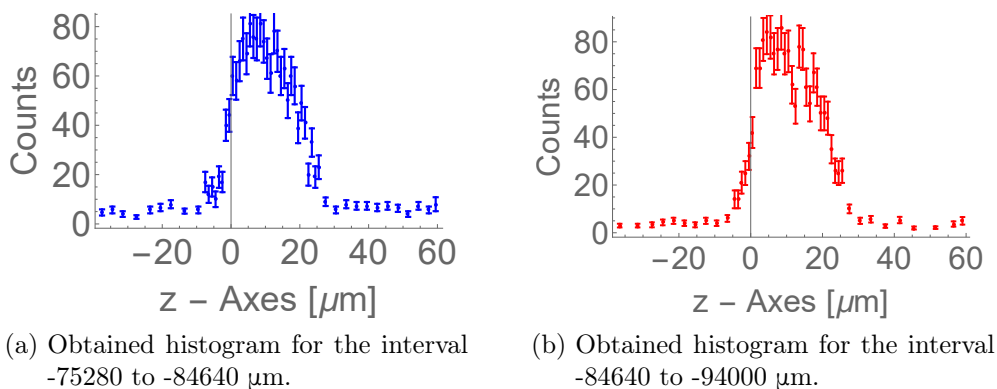(b) Obtained histogram for the interval -84640 to -94000 μm.

Figure 4.25: Obtained histogram for the interval approach

Table 4.7: Obtained values from fitting each interval with the wavefunctions and subsequently calculating the weighted mean for each value. Approach 2 for Detector ID 003.

$|C1|^2$ [%]	$48.0^{+4.7}_{-4.0}$
$|C2|^2$ [%]	$38.3^{+6.2}_{-7.3}$
$|C3|^2$ [%]	$13.7^{+7.4}_{-5.6}$
Spatial resolution [μm]	$3.21^{+0.33}_{-0.33}$
Absorber height [μm]	$40.14^{+1.69}_{-1.08}$

When comparing Table 4.4 with Table 4.7 one can see that the values, except

for the absorber height, are almost identical. This approach can be seen as a confirmation that the unbending process of the neutron track does not alter the outcome, since with this approach intervals with higher bending (i.e. higher standard deviation) are weighted considerably less in comparison to intervals with less bending.

4.3.3 Approach 3: Only take "actual" neutrons into account

When looking at the classifications obtained by the machine learning script in Section 4.3, one could argue that neutrons classified as "Candidate Extreme" contain far too many impurities, which may alter the result compared to classifications which are with most certainty neutrons. For this reason another wave function fit is done while only using neutrons from Figures 4.14(a)(b) and 4.15(a)(b), leaving 14111 neutrons without many impurities. The following steps, i.e. the unbending and spline interpolation, stays the same, resulting in the unbent neutron track shown in Figure 4.26.
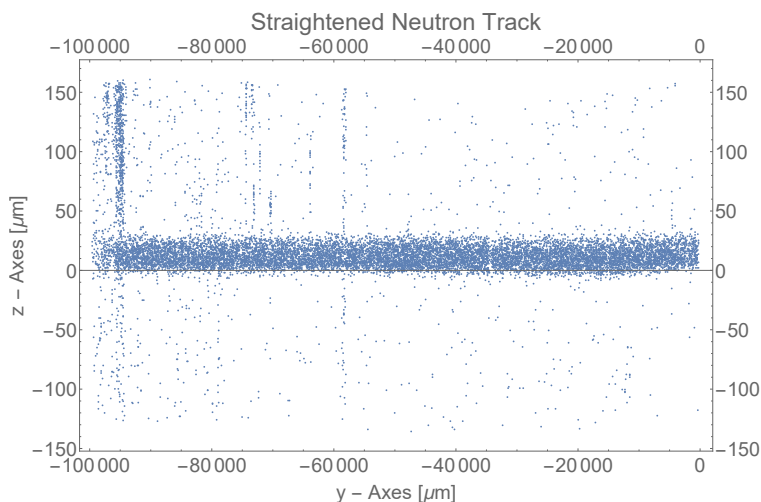

Figure 4.26: A plot of the straightened neutron track without the neutrons classified as "Candidate Extreme". 14111 neutrons are detected in total.

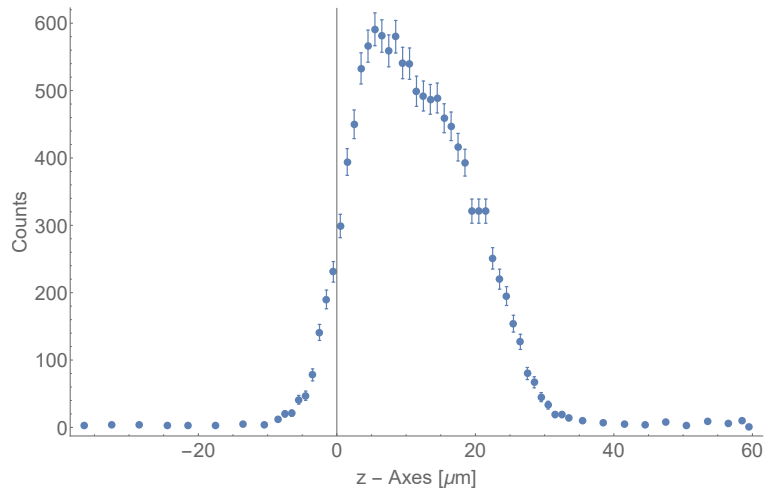The histogram obtained from this neutron track is shown in Figure 4.27.

Figure 4.27: A histogram obtained from the straight neutron track shown in Figure
4.26.

The values obtained from fitting this neutron track with 2 Airy functions are
shown in Table 4.8 and 4.9.

Table 4.8: Obtained values from fitting the histogram containing only 14111 neu-
trons as shown in Figure 4.27 with the first three eigenstates. The
reduced chi squared of this fit is $\chi^2 = 0.82$ with 41 DOF. Approach 3
for Detector ID 003.

$\|C1\|^2$ [%]	$47.5^{+1.2}_{-1.4}$
$\|C2\|^2$ [%]	$38.3^{+2.6}_{-2.2}$
$\|C3\|^2$ [%]	$14.2^{+3.1}_{-3.1}$
Spatial resolution [μm]	$3.65^{+0.08}_{-0.10}$
Absorber height [μm]	$31.00^{+0.75}_{-0.53}$

Table 4.9: Obtained values from fitting the histogram containing only 14111 neutrons as shown in Figure 4.27 with the first four eigenstates. The reduced chi squared of this fit is $\chi^2 = 0.83$ with 40 DOF. Approach 3 for Detector ID 003.

$|C1|^2$ [%]	$43.9^{+6.2}_{-3.7}$
$|C2|^2$ [%]	$34.6^{+9.0}_{-5.5}$
$|C3|^2$ [%]	$8.3^{+6.4}_{-5.3}$
$|C4|^2$ [%]	$13.2^{+21.4}_{-10.5}$
Spatial resolution [μm]	$3.5^{+0.22}_{-0.10}$
Absorber height [μm]	$29.96^{+1.28}_{-0.56}$

When comparing Table 4.4, 4.7 and 4.8, the best values for state occupation are almost identical, differing only in the size of the error interval. The approach with only 14111 neutrons has the smallest error bars. This can be explained by the fact that error bars do not solely rely on the number of neutrons, but also on how they are scattered around the z - Axis. The standard deviation highly depends on the sharpness of the edge at z = 0 μm. This fact leaves the only conclusion that taking more neutrons is not always better for statistics, but rather one should only take "actual", i.e. neutrons without any impurities, into account. By looking at table 4.9 and 4.5 one can see that the errors for the case of 14111 neutrons are significantly greater than for 21522 neutrons. The error bars for state $|4\rangle$ are almost twice as big as the error itself, which shows the clear limitations when using this script.

Nevertheless, when investigating the state occupation of an absorber-mirror configuration, it is best to decide which values to trust only after thoroughly studying many different approaches.

4.4 Region V, Detector ID L11

This detector was used to investigate the state occupation behind Region V. Unfortunately, the detector itself had visible scratches and was of poor quality. This results in fewer neutrons penetrating the boron layer and consequently fewer neutrons getting detected, which made any further analysis both more complicated and error-ridden. The raw data is shown in Figure 4.28.
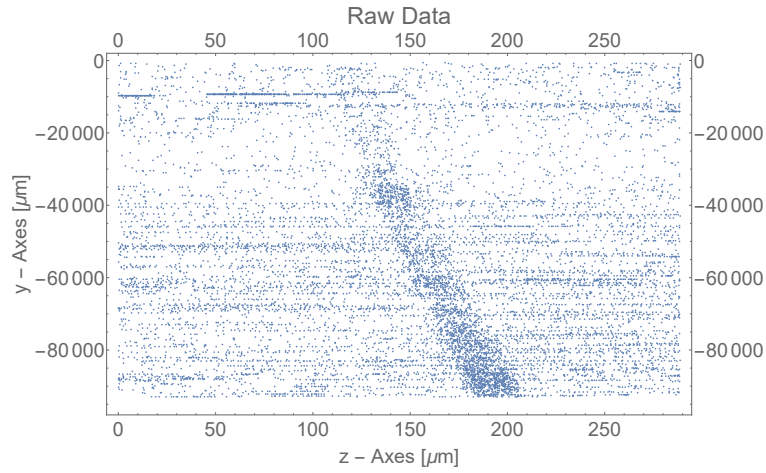
Figure 4.28: Raw data of the detected neutrons without any alteration. 11113 neutrons were detected in total.

The classified neutrons are shown in Figures 4.29 to 4.31. Note that for the sake of simplicity only classified neutrons with counts greater than 100 are shown.
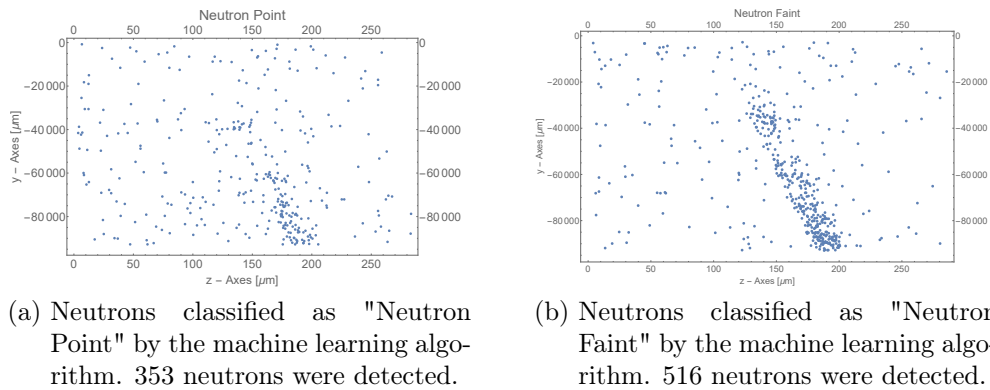

(a) Neutrons classified as "Neutron Point" by the machine learning algorithm. 353 neutrons were detected.
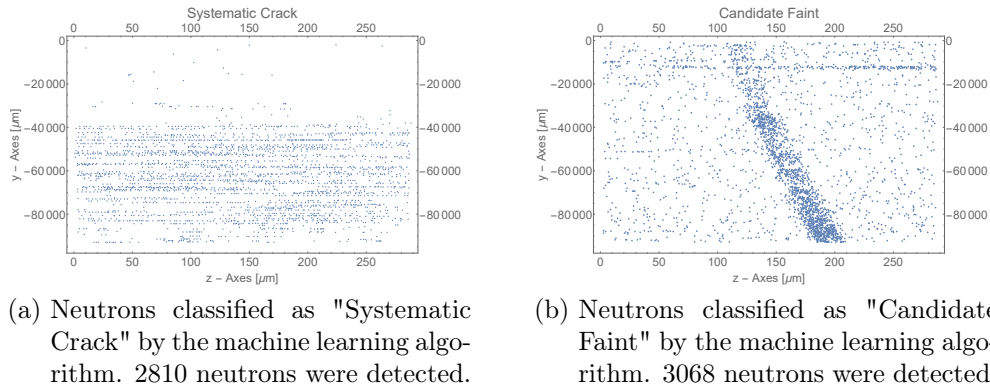
(b) Neutrons classified as "Neutron Faint" by the machine learning algorithm. 516 neutrons were detected.

Figure 4.29: Detected and classified neutrons by the machine learning algorithm.

(a) Neutrons classified as "Systematic Crack" by the machine learning algorithm. 2810 neutrons were detected.

(b) Neutrons classified as "Candidate Faint" by the machine learning algorithm. 3068 neutrons were detected.

Figure 4.30: Detected and classified neutrons by the machine learning algorithm.

(a) Neutrons classified as "Indeterminate" by the machine learning algorithm. 883 neutrons were detected.

(b) Neutrons classified as "Candidate Extreme" by the machine learning algorithm. 3123 neutrons were detected.
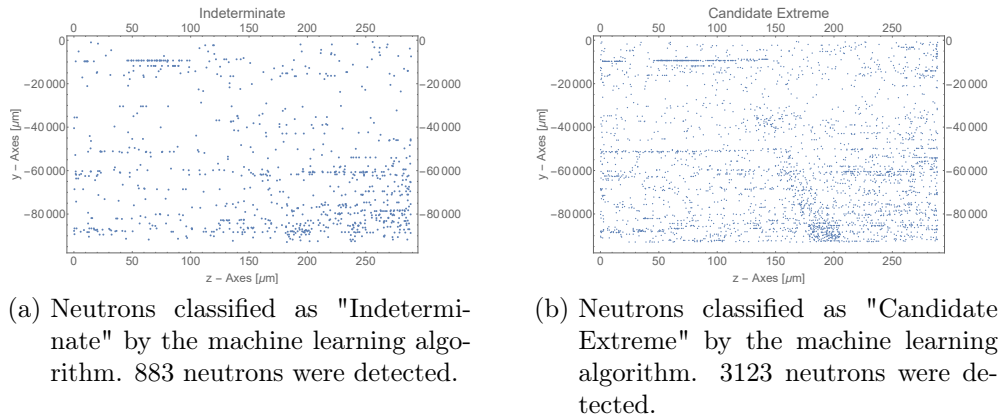
Figure 4.31: Detected and classified neutrons by the machine learning algorithm.

The chosen neutrons consist of neutrons classified as "Neutron Point", "Neutron Faint" and "Candidate Faint". In order to make the unbending process possible, the y range of the detector had to be cut from 30000 to $95000\mu m$. The final result is shown in Figure 4.32.
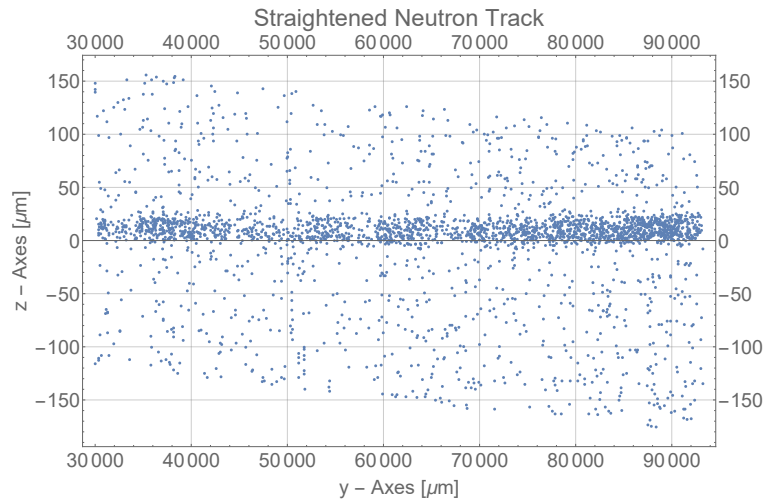
Straightened Neutron Track

Figure 4.32: Plot of the straightened neutron track. 2905 neutrons are remaining in total.

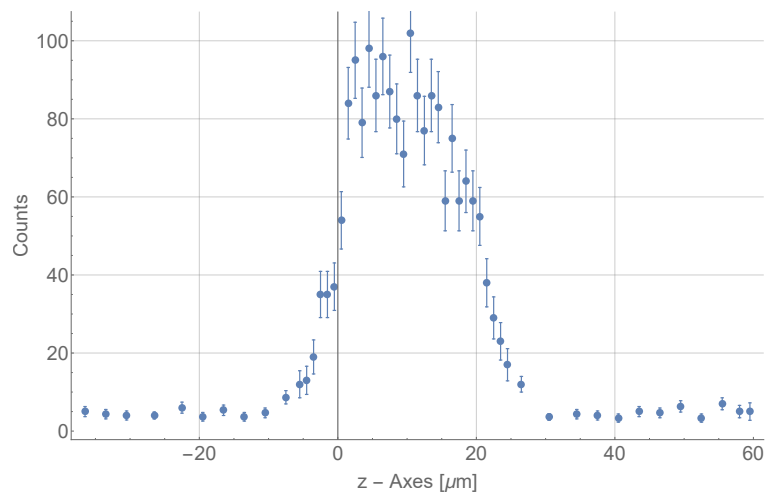The histogram made out of Figure 4.32 is shown in Figure 4.33.

Figure 4.33: Histogram obtained from the straight neutron track shown in Figure 4.32.

When comparing Figure 4.33 with Figure 4.20 the difference in the error bars is clearly visible. This is due to the fact that only 2905 neutrons are remaining compared to the 21522 neutrons from detector 003. The state occupation results are shown in Table 4.10 and 4.11.

Table 4.10: Obtained values from fitting the histogram containing 2905 neutrons as shown in Figure 4.33. Detector ID L11. The reduced chi squared of this fit is $\chi^2 = 1.06$ with 33 DOF.

$|C1|^2$ [%]	$43.2^{+4.7}_{-6.0}$
$|C2|^2$ [%]	$39.5^{+6.9}_{-6.1}$
$|C3|^2$ [%]	$17.3^{+2.0}_{-12.7}$
Spatial resolution [µm]	$3.60^{+0.25}_{-0.36}$
Absorber height [µm]	$27.38^{+2.44}_{-1.21}$

Table 4.11: Obtained values from fitting the histogram containing 2905 neutrons as shown in Figure 4.33. Detector ID L11. The reduced chi squared of this fit is $\chi^2 = 1.09$ with 32 DOF.

$|C1|^2$ [%]	$42.4^{+11.1}_{-14.3}$
$|C2|^2$ [%]	$40.6^{+6.9}_{-9.5}$
$|C3|^2$ [%]	$17.0^{+2.4}_{-11.6}$
$|C4|^2$ [%]	$0.0^{+11.2}_{-0.0}$
Spatial resolution [µm]	$3.35^{+0.35}_{-0.34}$
Absorber height [µm]	$27.75^{+2.68}_{-1.68}$

4.5 Region I+V, Detector ID 062/070

In this setup Region I and V were combined in order to measure the state occupation for state selector and analyzer. At the time of this thesis, CR39 detectors were rare and some had, as shown in section 4.4 Figure 4.28, many impurities like visible cracks and changing the colour under different angles, which means the coating material is not distributed homogeneously. This results in less neutrons getting detected. Either detector used for the final state occupation measurement, called 062 and 070, for Region I and V in series had many impurities on one half. Therefore these detectors were combined by putting the clear sides together, effectively creating one long CR39 detector. This step makes following analysis more conclusive. The following sections will explain how the y and z coordinates on the detectors were combined to obtain one coherent and straight neutron track.

4.5.1 Region I+V, Detector ID 062

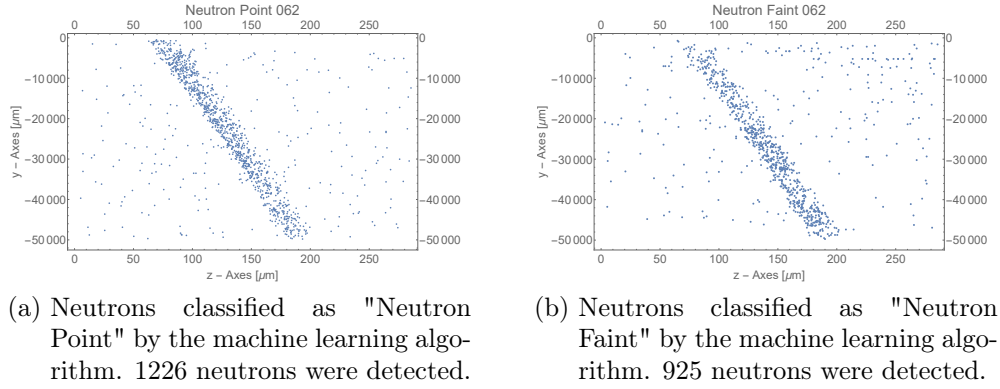The classification results for detector 062 are shown in Figures 4.34 to 4.36

(a) Neutrons classified as "Neutron Point" by the machine learning algorithm. 1226 neutrons were detected.
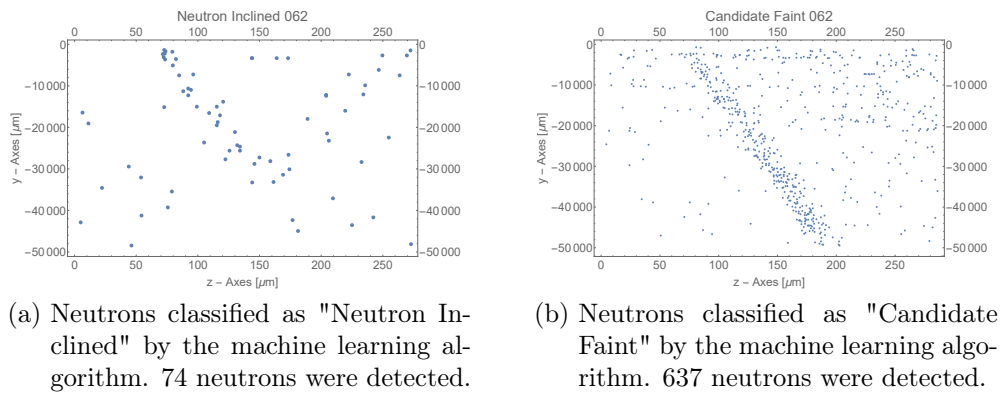
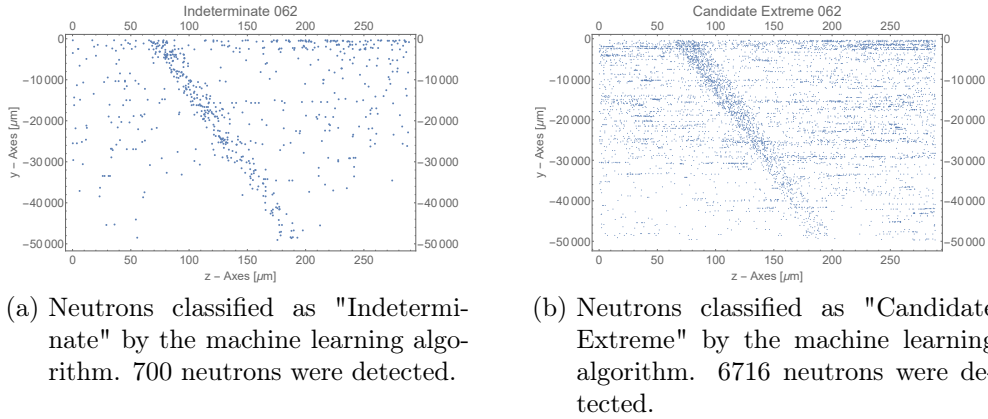(b) Neutrons classified as "Neutron Faint" by the machine learning algorithm. 925 neutrons were detected.
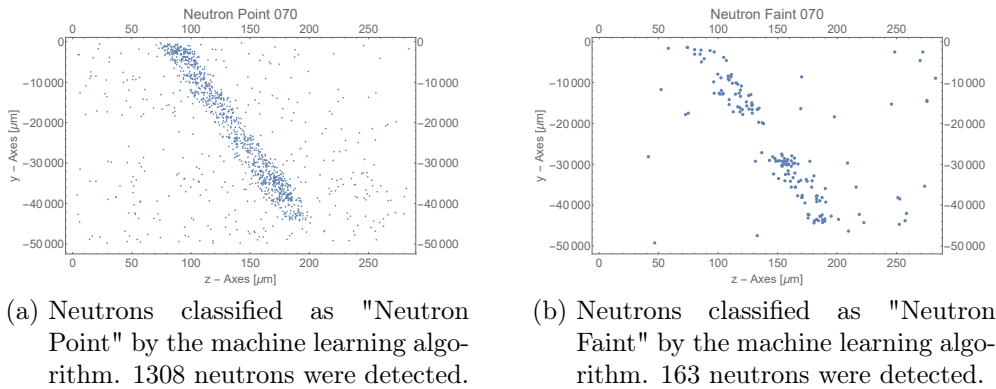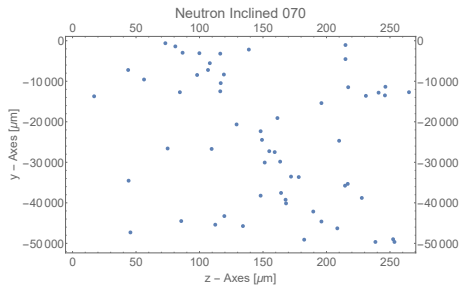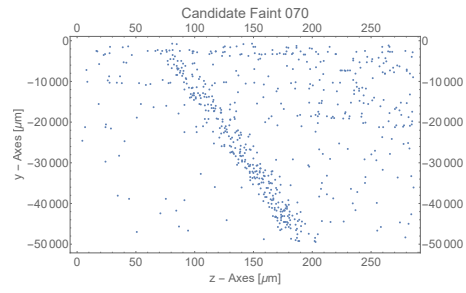
Figure 4.34: Detected and classified neutrons by the machine learning algorithm.

(a) Neutrons classified as "Neutron Inclined" by the machine learning algorithm. 74 neutrons were detected.

(b) Neutrons classified as "Candidate Faint" by the machine learning algorithm. 637 neutrons were detected.

Figure 4.35: Detected and classified neutrons by the machine learning algorithm.

(a) Neutrons classified as "Indeterminate" by the machine learning algorithm. 700 neutrons were detected.

(b) Neutrons classified as "Candidate Extreme" by the machine learning algorithm. 6716 neutrons were detected.

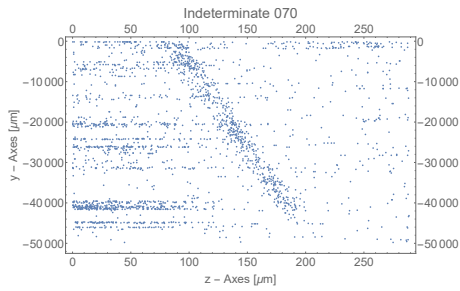Figure 4.36: Detected and classified neutrons by the machine learning algorithm.

The chosen neutrons consist of neutrons classified as "Neutron Point", "Neutron Faint", "Neutron Inclined", "Candidate Faint", "Indeterminate" and "Candidate Extreme". "Candidate Extreme" neutrons were chosen because of the great number classified as such, even though it might somewhat influence the end-result.

4.5.2 Region I+V, Detector ID 070

(a) Neutrons classified as "Neutron Point" by the machine learning algorithm. 1308 neutrons were detected.

(b) Neutrons classified as "Neutron Faint" by the machine learning algorithm. 163 neutrons were detected.

Figure 4.37: Detected and classified neutrons by the machine learning algorithm.

(a) Neutrons classified as "Neutron Inclined" by the machine learning algorithm. 58 neutrons were detected.
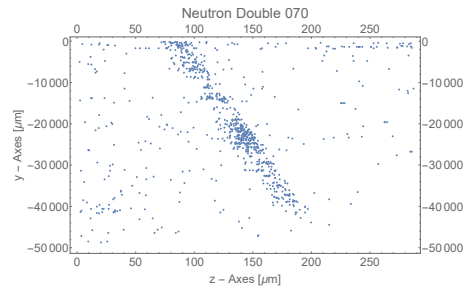
(b) Neutrons classified as "Candidate Faint" by the machine learning algorithm. 679 neutrons were detected.

Figure 4.38: Detected and classified neutrons by the machine learning algorithm.

(a) Neutrons classified as "Indeterminate" by the machine learning algorithm. 2223 neutrons were detected.

(b) Neutrons classified as "Neutron Double" by the machine learning algorithm. 854 neutrons were detected.

Figure 4.39: Detected and classified neutrons by the machine learning algorithm.

(a) Neutrons classified as "Systematic Dust by the machine learning algorithm. 3663 neutrons were detected.

(b) Neutrons classified as "Candidate Extreme" by the machine learning algorithm. 16136 neutrons were detected.
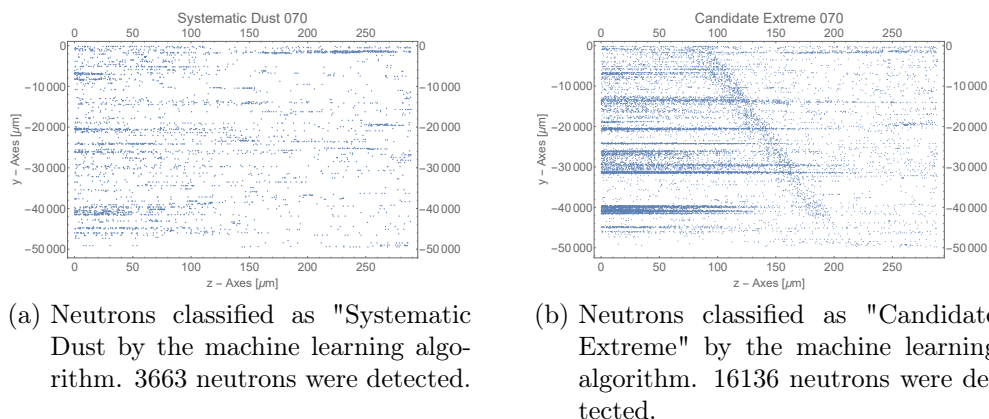
Figure 4.40: Detected and classified neutrons by the machine learning algorithm.

The chosen neutrons consist of neutrons classified as "Neutron Point", "Neutron Faint", "Neutron Inclined", "Candidate Faint" and "Indeterminate". Because of the many impurities on this detector, "Candidate Extreme" neutrons were excluded from further analysis.

4.5.3 Combining and straightening the neutron tracks

In order to be able to unbend the neutron track, it has be aligned parallel to the z-Axis. This is done by fitting the plot with a straight line, extracting the gradient (and subsequently the degree of the gradient) and rotating every (z, y) coordinate pair by the degree of the gradient. The combined result of these steps is shown in Figure 4.41.
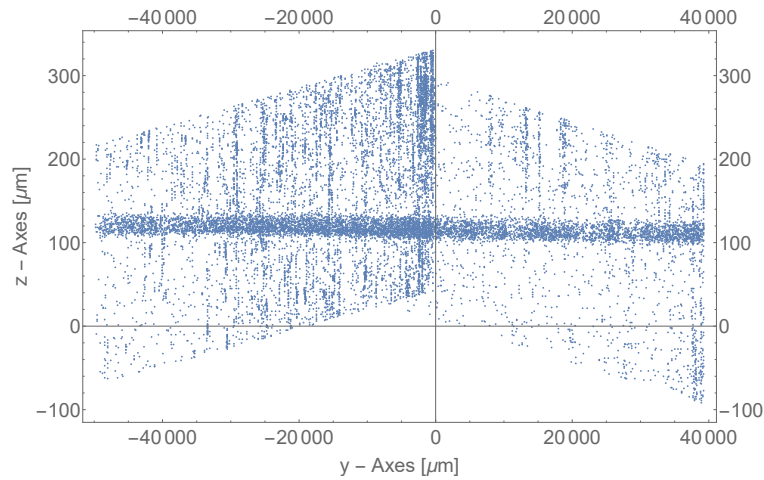
Figure 4.41: Plot of the combined and straightened neutrons from detector 062 and 070. Detector 070 is on the left and detector 062 on the right hand side. 15563 neutrons were detected in total.

Since the final result of Figure 4.41 is a histogram, it is evident that the z-Range has to be reduced in order to obtain a meaningful result. The z range was cut from 40 to 200 μm. The result is shown in Figure 4.42.
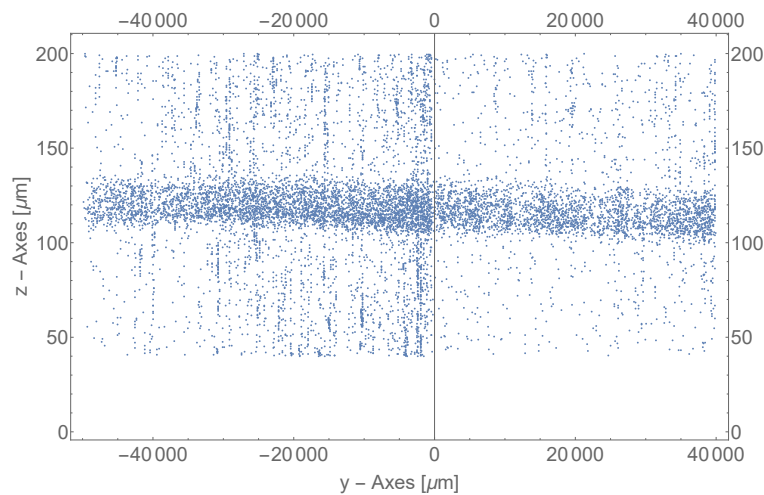

Figure 4.42: Plot of the combined neutrons from detector 062 and 070 where the z range is cut from 40 to 200 μm. 10559 neutrons were detected in total.

The next steps, i.e. the fitting of the error function and unbending it with spline interpolation, is the same as in the proceeding sections and one ends up with the straightened and unbent neutron track shown in Figure 4.43.
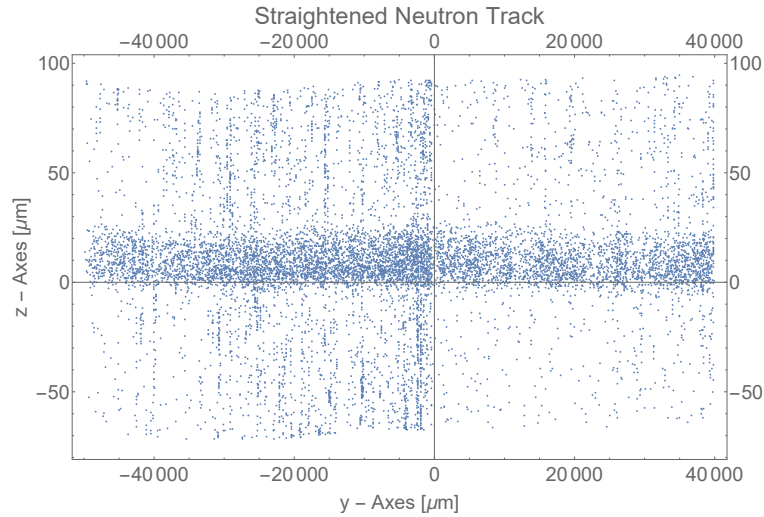

Figure 4.43: Plot of the straightened and unbent neutron track from detector 062 and 070.

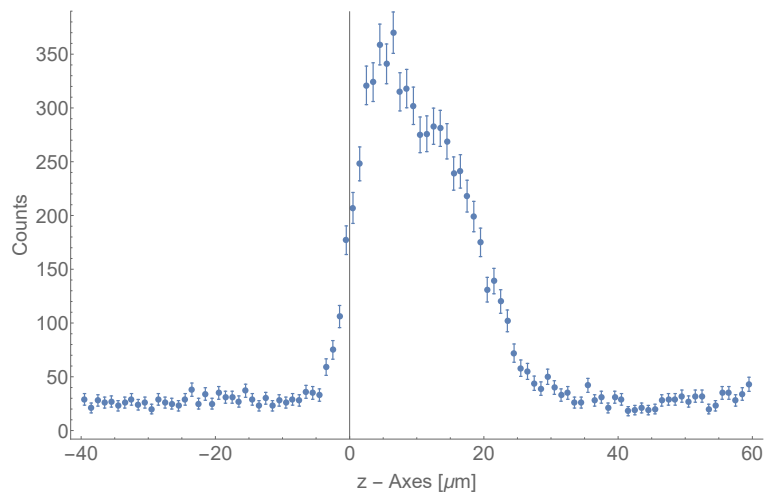The histogram obtained from Figure 4.43 is shown in Figure 4.44.

Figure 4.44: Histogram made out of the straight neutron track shown in Figure 4.43.

The final results of fitting this histogram with 2 Airy functions, analogous to the previous sections, are shown in Table 4.12 and 4.13.

Table 4.12: Obtained values from fitting the histogram containing 10559 neutrons as shown in Figure 4.44. Detector ID 062/070. The reduced chi squared of this fit is $\chi^2 = 0.93$ with 53 DOF.

$|C1|^2$ [%]	$60.7^{+2.2}_{-6.1}$
$|C2|^2$ [%]	$39.3^{+6.8}_{-2.0}$
$|C3|^2$ [%]	$0.0^{+4.0}_{-0.0}$
Spatial resolution [μm]	$2.53^{+0.15}_{-0.17}$
Absorber height [μm]	$34.25^{+17.82}_{-1.86}$

Table 4.13: Obtained values from fitting the histogram containing 10559 neutrons as shown in Figure 4.44. Detector ID 062/070. The reduced chi squared of this fit is $\chi^2 = 0.95$ with 52 DOF.

$|C1|^2$ [%]	$55.7^{+2.1}_{-2.2}$
$|C2|^2$ [%]	$43.7^{+5.7}_{-2.2}$
$|C3|^2$ [%]	$0.0^{+3.9}_{-0.0}$
$|C4|^2$ [%]	$0.7^{+11.6}_{-0.0}$
Spatial resolution [μm]	$2.53^{+0.14}_{-0.20}$
Absorber height [μm]	$34.10^{+0.0}_{-2.60}$

It is of interest to compare the results from measuring both detectors in series (Table 4.12 and 4.13) with the expected results when calculating the conjunct probabilities from both detectors separately (Tables 4.8 and 4.10 for three eigenstates and Tables 4.9 and 4.11 for four eigenstates). The normalized eigenstates of Region I and Region V combined can be calculated by multiplying the respective eigenstate probabilities and normalizing them:

$$|Ci|^2_{I+V} = \frac{|Ci|^2_I \times |Ci|^2_V}{C_{norm}}, \tag{4.4}$$

where $i = 1, 2, 3$ and $C_{norm} = |C1|^2_I \times |C1|^2_V + |C2|^2_I \times |C2|^2_V + |C3|^2_I \times |C3|^2_V$ for three eigenstates and $i = 1, 2, 3, 4$ and $C_{norm} = |C1|^2_I \times |C1|^2_V + |C2|^2_I \times |C2|^2_V + |C3|^2_I \times |C3|^2_V + |C4|^2_I \times |C4|^2_V$ for four eigenstates respectively.

The normalized state occupations are listed in Table 4.14 and 4.15.

Table 4.14: Obtained values for the state occupation when calculating the conjoint probabilities of detector 003 and detector L11 with three eigenstates. Values taken from Table 4.8 and 4.10.

	Combined probabilities
$\lvert C1 \rvert^2_{I+V}$ [%]	53.8
$\lvert C2 \rvert^2_{I+V}$ [%]	39.8
$\lvert C3 \rvert^2_{I+V}$ [%]	6.4

Table 4.15: Obtained values for the state occupation when calculating the conjoint probabilities of detector 003 and detector L11 with four eigenstates. Values taken from Table 4.9 and 4.11.

	Combined probabilities
$\lvert C1 \rvert^2_{I+V}$ [%]	54.6
$\lvert C2 \rvert^2_{I+V}$ [%]	41.2
$\lvert C3 \rvert^2_{I+V}$ [%]	4.1
$\lvert C4 \rvert^2_{I+V}$ [%]	0.0

The values in table 4.14 and 4.15 do not include errors. The reason lies in the fact that the errors for both Region I and V are asymmetric, thus Gaussian error propagation is not allowed (since this only accounts for a symmetric chi squared parabola, which is not the case).

These final results, when compared to Table 4.12 and 4.13, lie well within the margin of error and once more underline the robustness of the tools used.

5 Conclusion and Prospect

Within this master thesis four detectors have been successfully analyzed using Mathematica scripts written by Hanno Filter, Martin Thalhammer and Tobias Jenke. These scripts play an important role both in preparing as well as interpreting the results from the state occupation measurements correctly. The obtained results draw a pretty clear picture of what happens at each region of Ramsey's spectroscopy setup. This helps the experimenter later on to anticipate the results from Ramsey spectroscopy. By knowing the initial state occupations one is able to calculate the expected transition probabilities more correctly and compare them with the experimental data on a more fundamental level.

By investigating how the classification results are altered by varying etching time, as is done in Section 3.1, one gets a better understanding of how the events are classified and the importance of a right etching time. At a certain time the "Neutron Points" begin to merge and more "Neutron Doubles" are identified, which of course should be avoided. As optimal etching time I would recommend about 5 hours.

The results from Section 4.3 show the robustness of the data when evaluating it with different approaches. It also demonstrates the usefulness of the classification script when handling detectors with many impurities. These impurities can mostly be cut out by simply using clean classification results. Although the results do not drastically change when taking more or fewer neutrons into account, as shown in 4.3, the analysis should only be carried out with "actual" neutrons in order to guarantee the best fitting result. In order to make a satisfying result possible, one should take at least 3000 neutrons into account.

By comparing the results from Region I + V with the conjunct probabilities from each Region separately, as is done in Section 4.5.3, a clear overlap of the results within the margin of error is visible. This important outcome highlights the robustness when evaluating the data with the Mathematica scripts and furthermore validates the somewhat lengthy process of obtaining the state occupation distribution.

Bibliography

[1] A. Einstein, *Die Feldgleichungen der Gravitation*, Preuss. Akad. Wiss. Berlin, 1915.

[2] E. Corbelli, P. Salucci, *The Extended Rotation Curve and the Dark Matter Halo of M33*, Monthly Notices of the Royal Astronomical Society, 311 (2): 441–447, 2000.

[3] F. Zwicky, *Die Rotverschiebung von extragalaktischen Nebeln*, Helv. Phys. Acta, II(6):110, 1933.

[4] V. Trimble, *Existence and nature of dark matter in the universe*, doi: 10.1146/annurev.astro.25.1.425., 1987.

[5] J. E. Moody, F. Wilczek, *New macroscopic forces?*, Physical Review D, 30(1):130-138, 1984.

[6] J. Khoury, A. Weltman, *Chameleon Cosmology*, Phys. Rev. D 69, 044026, 2004.

[7] H. Abele, T. Jenke, H. Leeb, and J. Schmiedmayer, *Ramsey's method of separated oscillating fields and its application to gravitationally induced quantum phase shifts*, Physical Review D 81, 065019, p. 5, 2010.

[8] V. I. Lushchikov, *Quantum effects occuring when ultracold neutrons are stored on a plane*, JETP Letters, 28:559-561, 1978.

[9] V. V. Neszvizhevsky, *Quantum states of neutrons in the Earth's gravitational field*, Nature 415, 297-299, 2002.

[10] H. Wallis, J. Dalibard, and C. Cohen-Tannoudji, *Trapping Atoms in a Gravitational Cavity*, Appl. Phys. B 54, 407-419.

[11] Public Domain , Institute Laue Langevin, *https://www.ill.eu/users/instruments/instruments-list/pf2/description/instrument-layout/*, lastly visited on 26.05.2018.

[12] H. Abele, H. Leeb, *Atom- Kern- Und Teilchenphysik II*, p. 9, 2014.

[13] Tobias Jenke, Gunther Cronenberg, Hanno Filter, Hartmut Abele, *Ultracold neutron detectors based on 10B converters used in the qBounce experiments*, DOI: 10.1016/j.nima.2013.06.024

[14] H. Filter, *Miniforschung: Neutronendetektor auf CR-39 Basis*, 2009.

[15] J. M. Pendlebury, *A Revised Experimental Upper Limit on the Electric Dipole Moment of the Neutron*, Physical Review D 92, 092003, 2015.

[16] T. Jenke, *Weiterentwicklung eines Experiments zur Realisierung eines Quantum Bouncing Balls und Suche nach Extradimensionen der Raumzeit*, Diplomathesis, 2008.

[17] T. Rechberger, *Ramsey Spectroscopy of Gravitationally Bound Quantum States of Ultracold Neutrons*, Dissertation, 2018.

[18] I. I. Rabi, *A New Method of Measuring Nuclear Magnetic Moment*, Physical Review 53, 1938.

[19] T. Jenke, *qBounce - vom Quantum Bouncer zur Gravitationsresonanzspektroskopie*, Dissertation, 2011.

[20] G. Cronenberg, *Frequency Measurements to test Newton's Gravity Law within the qBounce experiment*, Dissertation, 2015.

[21] H.Abele, G. Cronenberg, P. Geltenbort, T. Jenke, T. Lins, H. Saul, *qBounce, the Quantum Bouncing Ball Experiment*, doi : 10.1016/j.phpro.2011.06.011.

[22] , T. Jenke, P. Geltenbort, H. Lemmel, H. Abele, *Realization of a gravity-resonance-spectroscopy technique*, Nature Physics volume 7, pages 468–472 (2011).

[23] N. F. Ramsey, *A Molecular Beam Resonance Method with Separated Oscillating Fields*, Physical Review 78, 1950.

[24] H. Abele, *Ramsey's method of separated oscillating fields and its application to gravitationally induced quantum phase shifts*, 2009.

[25] N. F. Ramsey, *Experiments with separated oscillatory fields and hydrogen masers*, Nobel Lecture, p. 558, 1989.

[26] H. Filter, *Interference Experiment with Slow Neutrons: A Feasibility Study of Lloyd's Mirror at the Institute Laue-Langevin*, Dissertation, 2018.

Acknowledgements